Acoustic wave propagation in permeable lossy metamaterials

Rodolfo Venegas[*] and Gabriel Núñez[†]

University Austral of Chile, Institute of Acoustics,

P.O. Box 567, Valdivia 5110701, Chile

Claude Boutin[‡]

Université de Lyon - Ecole Nationale des Travaux Publics de l'Etat,

LGCB / LTDS UMR-CNRS 5513 / CeLyA,

Rue Maurice Audin, Vaulx-en-Velin 69518, France

Olga Umnova[§]

Acoustics Research Centre, University of Salford, Salford M5 4WT, United Kingdom

Qicheng Zhang (张起成)[¶]

Key Laboratory of Artificial Micro- and Nano-Structures of

Ministry of Education and School of Physics and Technology,

Wuhan University, Wuhan 430072, China

(Dated: January 5, 2022)

1

Abstract

This paper investigates acoustic wave propagation in gas-saturated permeable lossy metamaterials which have different types of resonators, namely acoustic and elastic resonators, as building-block elements. By using the two-scale asymptotic homogenization method, the macroscopic equations that govern sound propagation in such metamaterials are established. These equations show that the metamaterials can be modelled as equivalent fluids with unconventional effective density and compressibility. Analysis of these frequency-dependent and complex-valued parameters shows that the real parts of both can take negative values within frequency bands determined by inner resonances. The upscaled theory is exemplified with the case of a permeable lossy metamaterial having a unit cell comprising two unconnected fluid networks and a solid frame. One of these fluid networks is loaded with acoustic resonators (e.g. quarter-wavelength, Helmholtz resonators) while thin elastic films are present in the other one. It is shown that the propagation of acoustic waves in permeable lossy metamaterials is determined by both classical visco-thermal dissipation and local elasto-inertial resonances. The results are expected to lead to judicious designs of acoustic materials with peculiar properties including negative phase velocity and phase constant characteristic for regressive waves, very slow phase velocity, and wide sub-wavelength band gaps.

Keywords: Acoustic metamaterials; equivalent fluid; homogenization; inner resonances; regressive waves.

———
* Corresponding author: rodolfo.venegas@uach.cl

† gabriel.nunez@alumnos.uach.cl

‡ claude.boutin@entpe.fr

§ o.umnova@salford.ac.uk

¶ qicheng.zhang@whu.edu.cn

I. INTRODUCTION

Metamaterials are artificially structured materials with atypical effective parameters that are primarily determined by the metamaterials' microstructure instead of chemical composition. Research on acoustic metamaterials, reviewed in [1–3], has rapidly grown since the works by Liu et al. [4] and Fang et al. [5] who reported, respectively, acoustic metamaterials exhibiting negative real part of the effective density and compressibility in a narrow frequency band. In both cases, this is due to the resonant behavior of the metamaterial constituents; with consequences being the existence of sub-wavelength bandgaps (i.e. frequency bands where wave propagation is forbidden), slow phase velocity, and high levels of sound attenuation. A negative real part of the effective parameters indicates an out-of-phase response. For example, in a material with negative real part of the effective density, the movement of the equivalent continuum is in the opposite direction to the driving force; while in a material with negative real part of the effective compressibility, the equivalent continuum expands upon an exerted pressure. Acoustic metamaterials exhibiting simultaneous negative real part of the effective density and compressibility have also been investigated in a number of works, e.g. [6–15]. Due to their peculiar properties, these so-called double-negative acoustic metamaterials have found application in, for example, sub-wavelength imaging [16–18] and realizing reverse Doppler effect [19, 20]. In addition, the last decade has seen a wealth of literature on acoustic metamaterials primarily intended for sound attenuation, with examples including waveguides loaded with resonators [21–25], coiled-space or labyrinthic metamaterials [26–30], arrays of membranes with added masses [31–33], arrays of Helmholtz resonators [34, 35], and permeo-elastic media [36, 37]. The atypical acoustical properties of most of these metamaterials rely on the resonant behavior of their constituents. Hence, the unconventional acoustic behavior is confined to narrow frequency bands. While this limitation could, at least in part, be overcome by visco-thermal losses, it is known that excessive losses can deteriorate the performance of acoustic metamaterials (see, e.g., [3, 38]). This clearly points out the need to properly account for losses in the modelling of acoustic metamaterials. This is done in this paper by using methods and analyses common for porous media acoustics [39–43]. For porous materials, the effects of losses have been widely studied, with examples being works on wave propagation in single porosity materials [44–48], such as arrays of pores (see, e.g., [49–53]), granular materials [54–59], fibrous materials [60–63], and

3

cellular materials [64–67]; multiscale porous media [59, 70–79]; and porous composites [80–83].

Air-saturated acoustic metamaterials with unit cells comprising thin elastic solids and acoustic resonators have been a subject of extensive research in recent years. Lee et al. [8] investigated wave propagation in a channel with interspaced clamped membranes and side holes. In this structure, which was built and tested, the identical membranes disconnected the fluid phase. The effective density and bulk modulus were modelled using a "lumped-element" approach while visco-thermal losses and fluid interaction with the membranes were not taken into account. In other words, the material was modelled as an equivalent loss-less fluid with real-valued effective properties that can simultaneously take negative values. While the experiments confirmed this assumption for the tested material, it was left to theoreticians to justify it. Similarly, Bongard et al. [9] investigated a one-dimensional structure comprising a channel with clamped membranes and transversally connected radial open channels. Using circuit theory and a transmission line approach, the membranes, which disconnected the channel's fluid network, were modelled as compliances while the open channels as shunt acoustic masses. The effects of visco-thermal losses were discarded due to the large characteristic size of the structure. The full-wave finite element simulations confirmed that the material exhibits negative, zero, or positive refractive index, depending on the frequency range. An acoustic double-negative metamaterial consisting of a channel with an array of interspaced clamped membranes and laterally loaded Helmholtz resonators was studied in [11]. As in the above mentioned works, the membranes rendered the channel's fluid network disconnected and visco-thermal losses were not considered. In this work, the possibility of simultaneous or separate negative effective density and bulk modulus was experimentally demonstrated. As in [9], these results were theoretically explained using both circuit theory and a transmission line approach. On the other hand, Lee and Wright [13] introduced the concept of hidden force and hidden source of volume to theoretically explain the negativity of the real-valued effective density or bulk modulus of a lossless material identical to that studied in [11]. Recently, Bellis and Lombard [15] used prototypical frequency-dependent expressions for the effective density and bulk modulus of a material with the same geometry as that studied in [11], in order to develop a time-domain model of sound propagation in a waveguide coupled with Helmholtz resonators and elastic membranes. The losses were described by a single lumped-type parameter in the expression for the complex-valued effec-

tive bulk modulus; while the effective density was considered to be a real-valued function. In all the works, mentioned in this paragraph, the single fluid network of the metamaterial was disconnected and the macroscopic equations that govern acoustic wave propagation in the metamaterial were directly postulated, instead of being derived using homogenization techniques. The latter implies that a recipe for the calculation of the effective parameters from the solution of boundary-valued problems that govern the local fluid physics is not yet available.

This paper investigates sound propagation in gas-saturated permeable lossy metamaterials with unit cells composed of a perfectly rigid and impervious solid domain and two fluid networks. The fluid that saturates one of the networks is in contact with the fluid that saturates an acoustic resonator (e.g. quarter-wavelength, Helmholtz resonator). The second fluid network contains a thin elastic film which strongly interacts with the fluid. Despite the presence of the film, the fluid network remains connected. One of the key contributions of this work is an upscaled theory of acoustic wave propagation in gas-saturated permeable lossy metamaterials. The macroscopic equations are derived using the two-scale asymptotic method of homogenization [43] and demonstrate that permeable lossy metamaterials can be modeled as equivalent fluids with complex-valued frequency-dependent effective parameters. These parameters describe the influence of local visco-elasto-inertial effects on the acoustical properties of the metamaterial. We also present i) a comprehensive analysis of the effective parameters of permeable lossy metamaterials, starting from a microscale description and unraveling the physical origin of their atypical acoustic behavior; and ii) an hybrid (numerical-analytical) model for exemplifying the unconventional acoustical properties of the metamaterials.

This work continues results on oscillatory fluid flow and heat conduction in single porosity media [44–48, 51–53, 67], double porosity media [59, 70–72], and porous composites [82, 83], as well as on oscillatory fluid-film interaction [36, 37]. The findings will be helpful in the bottom-up design of acoustic metamaterials for applications related to wave control and can be exploited together with the results of other works on oscillatory fluid flow in waveguides [84–87].

The paper is organized as follows. The macroscopic equations that govern sound propagation in permeable lossy metamaterials are established by homogenization in § II, with the details of the derivation being presented in the Appendix A. The asymptotic analysis

of the effective parameters of the metamaterial is presented in § III, while § IV introduces an hybrid model which is used in § V to exemplify key features of the effective parameters and acoustic behavior of permeable lossy metamaterials. Concluding remarks are presented in the last section of the paper.

II. ACOUSTIC WAVE PROPAGATION IN PERMEABLE LOSSY METAMATE-RIALS – THEORY

A.   Geometry and key assumptions

A generic geometry of the periodic acoustic metamaterials investigated in this work is shown in Figure 1. The representative elementary volume (REV) has a period l and comprises the domains $\Omega_b = \Omega_{bf} \cup \Omega_{br} \cup \Omega_{bs}$ and $\Omega_d = \Omega_{df} \cup \Omega_{ds}$. The perfectly-rigid solid part of the REV is $\Omega_s = \Omega_{bs} \cup \Omega_{ds}$ and its walls are $\Gamma_s = \Gamma_{bs} \cup \Gamma_{ds}$. An acoustic resonator Ω_{br}, such as a quarter-wavelength or a Helmholtz resonator (as in the diagram), is in contact with the fluid-saturated domain Ω_{bf} through the fluid-fluid interface Γ_{rf}. The thin elastic film Γ is clamped onto the perfectly-rigid and impervious solid domain Ω_{ds} and strongly interacts with the fluid that saturates Ω_{df}. Outward pointing normal vectors are denoted as $\mathbf{n}$ and $\mathbf{N}$. The macroscopic characteristic length L is related to the wavelength λ of the acoustic waves $\lambda = 2\pi L$. Throughout the paper, it is assumed both that $\lambda \gg l$, i.e. a long-wavelength regime is considered, and harmonic dependence of the type $e^{j\omega t}$. The former ensures a good separation of scales and allows defining a small parameter $\varepsilon = l/L \ll 1$.

It must be noted that since the gas-saturated parts of Ω_b and Ω_d, i.e. Ω_{bf} and Ω_{df}, are not connected, no interaction between the acoustic and elastic resonators is possible. The case where the resonators share a common fluid network and interact, either weakly or strongly, is beyond the scope of this work.

B.   Local governing equations

Acoustic wave propagation in Ω_{bf} is governed by the Stokes-Fourier system and boundary conditions of zero velocity and excess temperature on Γ_s as well as continuity of mass flux,
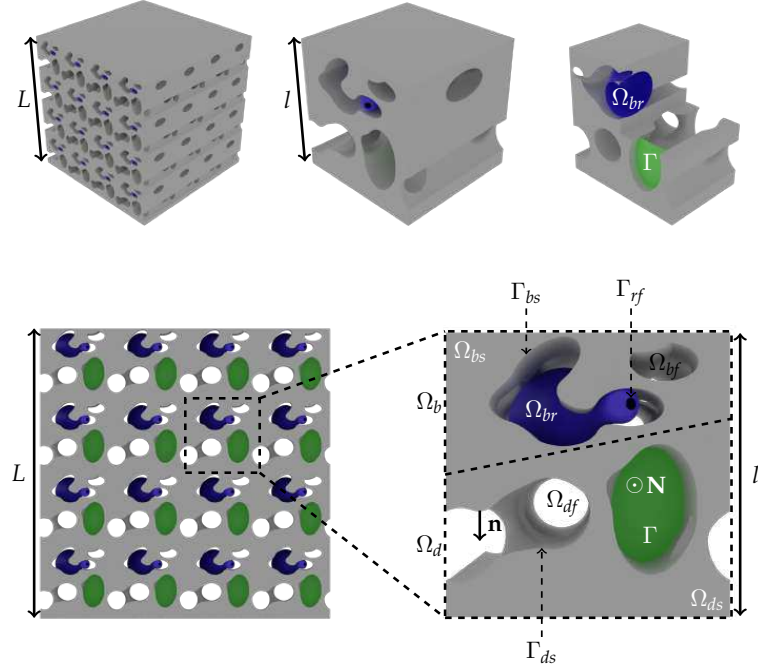
6

FIG. 1: Periodic geometry of a generic permeable lossy metamaterial. Top left – 3D macroscopic medium. Top middle – 3D Representative Elementary Volume (REV). Top right – Cutaway view of the 3D REV. Bottom left – 2D representation of the macroscopic medium. Bottom right – 2D representation of the REV. The clamped films Γ are shown in green, while the acoustic resonators Ω_{br} in blue. The solid frame in shown in gray and the pore fluid networks are transparent. (For interpretation of the references to color in this figure caption, the reader is referred to the web version of this article)

.

pressure, and temperature on Γ_{rf}, namely

$$\text{div}(2\eta\mathbf{D}(\mathbf{v}_b)) - \nabla p_b = \text{j}\omega\rho_0\mathbf{v}_b \quad \text{in} \quad \Omega_{bf}, \tag{1}$$

$$\text{j}\omega\rho_b + \rho_0\nabla \cdot \mathbf{v}_b = 0 \quad \text{in} \quad \Omega_{bf}, \tag{2}$$

$$\kappa\nabla \cdot \nabla\tau_b = \text{j}\omega\rho_0 c_p\tau_b - \text{j}\omega p_b \quad \text{in} \quad \Omega_{bf}, \tag{3}$$

7

$$\frac{p_b}{P_0} = \frac{\rho_b}{\rho_0} + \frac{\tau_b}{\tau_0} \quad \text{in} \quad \Omega_{bf}, \tag{4}$$

$$\mathbf{v}_b = \mathbf{0} \quad \text{on} \quad \Gamma_{bs}, \tag{5}$$

$$\tau_b = 0 \quad \text{on} \quad \Gamma_{bs}, \tag{6}$$

$$\rho_0 \mathbf{v}_b \cdot \mathbf{n} = \rho_0 \mathbf{v}_r \cdot \mathbf{n} \quad \text{on} \quad \Gamma_{rf}, \tag{7}$$

$$p_b = p_r \quad \text{on} \quad \Gamma_{rf}, \tag{8}$$

$$\tau_b = \tau_r \quad \text{on} \quad \Gamma_{rf}. \tag{9}$$

The physical parameters are the dynamic viscosity η, specific heat capacity c_p, thermal conductivity κ, and equilibrium pressure P_0, density ρ_0, and temperature τ_0. The unknown variables are the oscillating velocity $\mathbf{v}_b$, pressure p_p, density ρ_b, and temperature τ_b; while $\mathbf{D}(\mathbf{v}_b) = \frac{1}{2}(\nabla \mathbf{v}_b + (\nabla \mathbf{v}_b)^T - \frac{2}{3}\nabla \cdot \mathbf{v}_b \mathbf{I})$ is the deviatoric strain rate tensor, where $\mathbf{I}$ is the unitary second-rank tensor. Note also that $\mathbf{v}_r$, p_r and τ_r are, respectively, the fluid velocity, pressure, and temperature in the resonator, which as shown in Appendix A are not required to be specified.

The propagation of acoustic waves in the fluid-saturated part of the permeo-elastic domain, i.e. Ω_{df}, is governed by the Stokes-Fourier system Eqs.(10)–(13) coupled with Eqs. (14)–(16) that govern the dynamics of the clamped film. The film, modelled as a Love-Kirchhoff plate [36], can be pre-stressed, which means that bending and membrane effects are accounted for [37]. The system is completed with clamping boundary conditions formulated on $\partial\Gamma$, i.e. Eq. (18), and conditions of zero velocity and excess temperature on Γ_s, i.e. Eq. (19) and (20).

$$\text{div}(2\eta\mathbf{D}(\mathbf{v}_d)) - \nabla p_d = \text{j}\omega\rho_0\mathbf{v}_d \quad \text{in} \quad \Omega_{df}, \tag{10}$$

$$\text{j}\omega\rho_d + \rho_0\nabla \cdot \mathbf{v}_d = 0 \quad \text{in} \quad \Omega_{df}, \tag{11}$$

$$\kappa\nabla \cdot \nabla\tau_d = \text{j}\omega\rho_0 c_p\tau_d - \text{j}\omega p_d \quad \text{in} \quad \Omega_{df}, \tag{12}$$

$$\frac{p_d}{P_0} = \frac{\rho_d}{\rho_0} + \frac{\tau_d}{\tau_0} \quad \text{in} \quad \Omega_{df}. \tag{13}$$

$$\widetilde{\nabla} \cdot (\mathbf{T} + \mathcal{T}\widetilde{\nabla}u_d) = -\omega^2\rho_e t u_d - [\boldsymbol{\sigma}_d \cdot \mathbf{N}] \cdot \mathbf{N} \quad \text{on} \quad \Gamma \tag{14}$$

$$\mathbf{T} = -\widetilde{\text{div}}(\mathbf{M}) \quad \text{on} \quad \Gamma, \tag{15}$$

$$\mathbf{M} = EI\left((1-\nu)\widetilde{\mathbf{e}}(\widetilde{\nabla}u_d) + \nu\widetilde{\nabla} \cdot \widetilde{\nabla}u_d\mathbf{I}\right) \quad \text{on} \quad \Gamma, \tag{16}$$

8

$$\mathbf{v}_d = \mathrm{j}\omega u_d \mathbf{N} \quad \text{on} \quad \Gamma, \tag{17}$$

$$u_d = 0 \quad \text{and} \quad \widetilde{\nabla} u_d \cdot \mathbf{n} = 0 \quad \text{on} \quad \partial\Gamma. \tag{18}$$

$$\mathbf{v}_d = \mathbf{0} \quad \text{on} \quad \Gamma_{ds}, \tag{19}$$

$$\tau_d = 0 \quad \text{on} \quad \Gamma_{ds} \cup \Gamma. \tag{20}$$

The unknown variables in Eqs.(10)–(13) are analogous to those in Eqs. (1)–(4). In Eqs. (14)–(18), the tilde on the differential operators denotes that these act on the plane Γ. For instance, $\widetilde{\mathbf{e}}(\cdot) = (\widetilde{\mathrm{grad}}(\cdot) + \widetilde{\mathrm{grad}}^T(\cdot))/2$ is the symmetric part of the in-plane gradient operator. The out-of-plane shear stress vector $\mathbf{T}$ and the bending moment of the in-plane stress tensor $\mathbf{M}$ are integrated over the film thickness t. The "plate" modulus of the films is $E = \mathrm{E}/(1 - \nu^2)$, where E and ν are the Young's modulus and Poisson's ratio, respectively. The bending stiffness is EI, where $I = t^3/12$ is the moment of inertia of the plate. The surface density of the films is $\rho_e t$ and the thickness of the films satisfies $t \ll l$. In addition, the film is loaded by the action of the fluid on its faces and its own inertia, as represented by the right-hand side terms of Eq. (14). The former is the jump across Γ of the normal component of the fluid stress vector, i.e. $[\boldsymbol{\sigma}_d \cdot \mathbf{N}] \cdot \mathbf{N}$, where $[\cdot]$ represents the 'jump' across Γ (e.g. $[a] = a^+ - a^-$, with the superscript $^+$ and $^-$ representing the opposite faces of the film). Furthermore, it has been considered that the film has been isotropically and uniformly pre-stressed by $\boldsymbol{\sigma}_{\mathcal{T}} = \sigma_{\mathcal{T}}\mathbf{I} = (\mathcal{T}/t)\mathbf{I}$, where $\mathcal{T}$ is the uniform tension per unit length.

The two-scale asymptotic method of homogenization [43] is applied, as shown in the Appendix A, to the set of equations (1)–(20) in order to establish a macroscopic description of sound propagation in permeable lossy metamaterials. The general steps of the upscaling process are the analysis of the local physics, rescaling of the local description, searching of the unknown variables as series expansion in terms of the small parameter ε, identification of boundary-value problems, and determination of the effective macroscopic equations that govern the propagation of sound waves in permeable lossy metamaterials. The latter is presented in the next section.

C. Macroscopic equations and effective parameters

The macroscopic equations that govern sound propagation in permeable lossy metamaterials are the mass balance equation (21) and the fluid flow constitutive law (22) (see

Appendix A for their derivations), namely

$$\nabla \cdot \mathbf{V} = -\mathrm{j}\omega(p_b\phi_b\mathsf{C}_{br}(\omega) + p_d\phi_d\mathsf{C}_d(\omega)), \tag{21}$$

$$\mathbf{V} = -\frac{\phi_b\mathbf{k}_b(\omega)}{\eta}\cdot\nabla p_b - \frac{\phi_d\mathbf{k}_d(\omega)}{\eta}\cdot\nabla p_d, \tag{22}$$

where $\mathbf{V}$ and p_b and p_d represent the averaged fluid velocity and pressures in the permeable lossy metamaterial, respectively. The subscript in the differential operator and the superscript denoting the order in the variables have been dropped to ease the notation. The effective parameters of the model are described below.

Eqs. (21) and (22) demonstrate that the acoustic response of the investigated permeable lossy metamaterials is described by a two-pressure model. This is a consequence of the decoupled nature of the pore fluid networks Ω_{bf} and Ω_{df} and differs from classical single-pressure models for conventional, multiscale, or composite porous materials (see e.g. [42, 43, 77, 82, 83]). However, the acoustic response of permeable lossy metamaterials can be described by a single-pressure model under the following conditions. Consider a metamaterial layer for which its thickness is much smaller than the sound wavelengths $|\lambda_\iota|$ (with $\iota = b, d$) and, at the same time, larger than the metamaterial's period. In such a case, the pressure gradient, determined by the pressures at the extremities of the layer, is identical in both effective fluids. It then follows that the pressures p_b and p_d are also equal, i.e. $p_b = p_d = p$, and the two-pressure model can be reduced to the following single-pressure model that describes the apparent acoustic response of permeable lossy metamaterials:

$$\nabla \cdot \mathbf{V} = -\mathrm{j}\omega p\mathsf{C}(\omega), \tag{23}$$

$$\mathbf{V} = -\frac{\mathbf{k}(\omega)}{\eta}\cdot\nabla p. \tag{24}$$

Here, the effective compressibility C is given by (with $\phi_b = \Omega_{bf}/\Omega$ and $\phi_d = \Omega_{df}/\Omega$)

$$\mathsf{C}(\omega) = \phi_b\mathsf{C}_{br}(\omega) + \phi_d\mathsf{C}_d(\omega). \tag{25}$$

The effective compressibilities C_{br} and C_d read as (see § A 4 for their derivation)

$$\mathsf{C}_{br}(\omega) = \mathsf{C}_b(\omega) + \mathsf{C}_r(\omega), \tag{26}$$

$$\mathsf{C}_b(\omega) = \frac{1}{P_0}\left(1 - \frac{\gamma-1}{\gamma}\mathrm{j}\omega\rho_0 c_p\frac{\Theta_b(\omega)}{\kappa}\right), \tag{27}$$

$$\mathsf{C}_r(\omega) = \frac{2}{\mathcal{L}}\frac{\mathcal{Y}_r(\omega)}{j\omega}, \tag{28}$$

10

$$\mathsf{C}_d = \frac{1}{P_0} \left(1 - \frac{\gamma - 1}{\gamma} \mathrm{j}\omega \rho_0 c_p \frac{\Theta_d(\omega)}{\kappa} \right), \tag{29}$$

where the thermal permeabilities are calculated as $\Theta_\iota(\omega) = \langle \hat{\Theta}_\iota(y,\omega) \rangle_\iota$ (with $\iota = b, d$, see also §A 3 b), $\mathcal{L} = 2\Omega_{bf}/\Gamma_{rf}$ is a characteristic length, and $\mathcal{Y}_r(\omega)$ is the effective admittance of the resonator. Exact expressions for the admittance depending on the type of the resonator are presented in the Appendix B.

The dynamic visco-elasto-inertial permeability tensor $\mathbf{k}(\omega)$ is given by

$$\mathbf{k}(\omega) = \phi_b \mathbf{k}_b(\omega) + \phi_d \mathbf{k}_d(\omega), \tag{30}$$

where the dynamic visco-inertial permeability of the effective fluid saturating Ω_{bf}, i.e. $\mathbf{k}_b$, and the dynamic visco-elasto-inertial permeability of the effective fluid saturating Ω_{df}, i.e. $\mathbf{k}_d$, are given by

$$\mathbf{k}_b(\omega) = \langle \hat{\mathbf{k}}_b(y,\omega) \rangle_b \quad \text{and} \quad \mathbf{k}_d(\omega) = \langle \hat{\mathbf{k}}_d(y,\omega) \rangle_d, \tag{31}$$

where $\hat{\mathbf{k}}_b(y,\omega)$ and $\hat{\mathbf{k}}_d(y,\omega)$ are calculated from the solution of the boundary-value problems detailed in § A 3 a and § A 3 c, respectively.

On the other hand, the effective density tensor $\boldsymbol{\rho}$ is related to the visco-elasto-inertial permeability tensor through

$$\boldsymbol{\rho}(\omega) = \frac{\eta}{\mathrm{j}\omega} \mathbf{k}^{-1} = (\phi_b \boldsymbol{\rho}_b^{-1} + \phi_d \boldsymbol{\rho}_d^{-1})^{-1}, \tag{32}$$

where $\boldsymbol{\rho}_b = \eta \mathbf{k}_b^{-1}/\mathrm{j}\omega$ and $\boldsymbol{\rho}_d = \eta \mathbf{k}_d^{-1}/\mathrm{j}\omega$.

For the analyses and examples to be presented in the next sections, it is pertinent to recall that the effective wave number $k_c(\omega)$ and speed of sound $c(\omega)$ are given by

$$k_c = \omega\sqrt{\rho(\omega)\mathsf{C}(\omega)} = \omega|\rho(\omega)|^{1/2}|\mathsf{C}(\omega)|^{1/2}e^{\mathrm{j}\theta_k(\omega)}, \tag{33}$$

$$c(\omega) = \frac{\omega}{k_c(\omega)} = \frac{e^{\mathrm{j}\theta_c(\omega)}}{|\rho(\omega)|^{1/2}|\mathsf{C}(\omega)|^{1/2}}. \tag{34}$$

These expressions are valid for macroscopically isotropic metamaterials or when considering a preferential sound propagation direction (i.e. the effective density tensor becomes $\boldsymbol{\rho}(\omega) = \rho(\omega)\mathbf{I}$), and $\theta_\rho(\omega)$ and $\theta_{\mathsf{C}}(\omega)$ are the frequency-dependent phases of the effective density and compressibility, respectively.

The phase of the effective speed of sound and wave number are respectively given by

$$\theta_c(\omega) = -\frac{\theta_\rho(\omega) + \theta_{\mathsf{C}}(\omega)}{2} \quad \text{and} \quad \theta_k(\omega) = -\theta_c(\omega). \tag{35}$$

In summary, the two-pressure model [Eqs. (21) and (22)] and its reduction to a single-pressure model [Eqs. (23) and (24)] are the main contributions of this paper. The latter model shows that a permeable lossy metamaterial can be modelled as an equivalent fluid with effective complex-valued frequency-dependent parameters $\mathbf{k}$ and C. Specifically, Eq. (23) demonstrates that the effective compressibility depends on the classical effective compressibilities of the fluid saturating the pore fluid networks, i.e. C_b and C_d which are determined by the losses caused by the thermal exchanges between the saturating fluid and the solid frame of the material, and an apparent compressibility, i.e. C_r, that accounts for the influence of the identical acoustic resonators through the effective admittance $\mathcal{Y}_r$. It is the latter that induces atypical acoustic behavior, as it will be shown in § III where the properties of the effective compressibility are analyzed in detail. On the other hand, despite the formal similarity between Eq. (24) and the dynamic Darcy's law [44], Eq. (24) does not correspond to such a law [36, 37]. This is because the elastic and inertial effects in the films as well as the viscous and inertial effects in both pore fluid networks affect $\mathbf{k}$. The interplay between these effects also contributes to an atypical behavior of the medium, as will be shown later in the paper.

To conclude this section, it is worth highlighting degenerate cases of the upscaled model given by Eqs. (23) and (24). If the acoustic resonators are not present and the films are absent or can be considered as perfectly rigid, the upscaled model reduces to that of wave propagation in double porosity materials with weakly contrasted permeabilities [72]. If the permeo-elastic channel is absent, i.e. $\phi_d = 0$, the resulting upscaled model is that of wave propagation in a fluid-saturated array of resonators [34, 35]. If the resonators are replaced by a perfectly rigid impermeable solid, the upscaled model for wave propagation in single porosity materials [44, 48] is retrieved, which is also the case if $\phi_b = 0$ and the films are perfectly rigid. On the other hand, if $\phi_b = 0$, then the upscaled model for wave propagation in permeo-elastic media [36, 37] is retrieved. In addition, the upscaled model introduced in this work degenerates to that of wave propagation in porous composites with weakly contrasted permeabilities [82] if ϕ_d and ϕ_b are the volume fractions of the porous constituents and the effective parameters C_d, $\mathbf{k}_d$, C_b, and $\mathbf{k}_b$ are interpreted as those of the porous constituents b and d accordingly.

12

III.   ANALYSIS OF THE EFFECTIVE ACOUSTIC PROPERTIES

Here, the low- and high-frequency behavior of the effective parameters is investigated, together with that at several characteristic frequencies. As previously, a preferential sound propagation direction is considered for simplicity. Hence, the tensors are replaced by the scalars $\mathcal{K}$, $\mathcal{K}_b$, $\mathcal{K}_d$, ρ, ρ_b, and ρ_d, which can represent the norms of the respective tensors. Such approximation is valid for isotropic or even moderately anisotropic metamaterials.

In what follows, the frequency-dependent terms, derived in the Appendix C, that link the local fields and the effective parameters will be used for the analysis. For the oscillatory flows, these correspond to $\mathcal{V}_b = \Re(\mathcal{K}_b)$ and $\mathcal{I}_b = -\Im(\mathcal{K}_b)$, which reflect the dissipated viscous and kinetic energy in Ω_{bf}, respectively; and to $\mathcal{V}_d = \Re(\mathcal{K}_d)$, $\mathcal{E}_d$, and $\mathcal{I}_d$ which reflect, respectively, the dissipated viscous, elastic, and kinetic energies in Ω_{df}. These are strongly affected by the fluid-film interaction. Note also that $\mathcal{E}_d$ is determined by the elasticity of the films, $\mathcal{I}_d$ is affected by the inertia of both the fluid and the films, and $\Im(\mathcal{K}_d) = \mathcal{E}_d - \mathcal{I}_d$. For the oscillatory temperature fields, these correspond to $\mathcal{H}_\iota = (\gamma - 1)\Re(\Theta_\iota)/\gamma\delta_t^2$ and $\mathcal{S}_\iota = -(\gamma - 1)\Im(\Theta_\iota)/\gamma\delta_t^2$ (with $\iota = d, b$), where $\mathcal{S}_\iota$ and $\mathcal{H}_\iota$ reflect the stored and dissipated (due to heat conduction) energies, respectively.

A.   Effective dynamic permeability and density

The dynamic visco-inertial permeability $\mathcal{K}_b$ behaves classically. Hence, it tends to

$$\mathcal{K}_b(\omega \ll \omega_{vb}) \to \mathcal{K}_b(\omega = 0) = \mathcal{K}_{0b} \quad \text{and} \quad \mathcal{K}_b(\omega \gg \omega_{vb}) \to -\mathrm{j}\frac{\delta_v^2}{\alpha_{\infty b}}, \tag{36}$$

where $\omega_{vb} = \nu/\mathcal{K}_{0b}\alpha_{\infty b}$, $\mathcal{K}_{0b}$, and $\alpha_{\infty b}$ are the viscous characteristic (or Biot) frequency, static viscous permeability, and tortuosity of the pore fluid network Ω_{bf}, respectively. The boundary layer thickness is $\delta_v = \sqrt{\nu/\omega}$, where ν is the kinematic viscosity of the saturating fluid. Let us recall that the Biot frequency determines the transition from viscosity- and inertia-dominated oscillatory flow in the pore space Ω_{bf} and indicates the frequency at which the dissipation of sound due to the viscosity of the fluid saturating the said pore space is maximized. Moreover, at the Biot frequency one has that $\mathcal{I}_b(\omega_{vb}) = \mathcal{V}_b(\omega_{vb})$.

Then, the magnitude and phase of the dynamic density ρ_b tend to

$$|\rho_b(\omega \ll \omega_{vb})| \to \rho_0 \frac{\delta_v^2}{\mathcal{K}_{0b}} \quad \text{and} \quad |\rho_b(\omega \gg \omega_{vb})| \to \rho_0 \alpha_{\infty b}, \tag{37}$$

13

$$\theta_{\rho b}(\omega \ll \omega_{vb}) = -\frac{\pi}{2} \quad \text{and} \quad \theta_{\rho b}(\omega \gg \omega_{vb}) \to 0. \tag{38}$$

The dynamic visco-elasto-inertial permeability $\mathcal{K}_d$ has a complex behavior in frequency, as discussed in detail in [36, 37]. Several characteristic frequencies can be defined as follows. The visco-inertial characteristic frequency ω_{vd} determines the transition from viscous- to inertia-dominated flow. Note, however, that ω_{vd} is defined, in the absence of elastic effects (i.e. $\mathcal{E}_d \to 0$), implicitly through $\mathcal{V}_d(\omega_{vd}) = \mathcal{I}_d(\omega_{vd})$. Similar to classical porous media, an estimation of this frequency is $\omega_{vd} = \nu/\mathcal{K}_{0d}\alpha_{\infty d}$. In this expression, $\mathcal{K}_{0d} = \mathcal{V}_d(\omega \to 0)$ is the static permeability, which is well approximated by that of material with same geometry as that of the permeo-elastic one but with perfectly rigid instead of elastic films; and $\alpha_{\infty d} = \delta_v^2 \mathcal{I}_d^{-1}(\omega \gg \omega_{vd})$ is the respective tortuosity, which is affected by the fluid-film interaction [36, 37]. Then, the limiting behavior of $\mathcal{K}_d$ is formally similar to that shown in Eq. (36) but with the subscript $b \to d$. Consequently, the magnitude and phase of ρ_d tend to the values quoted in Eq. (37) and Eq. (38) (with $b \to d$), respectively.

On the other hand, elasto-inertial characteristic frequencies which correspond to an anti-resonance frequency ω_{ad} and a resonance frequency ω_{gd} can be defined [36, 37] when viscous effects are negligible (i.e. when $\mathcal{V}_d \to 0$). In both cases, the elastic energy is compensated by the kinetic energy, which means that ω_{ad} and ω_{gd} are both implicitly defined through $\mathcal{E}_d = \mathcal{I}_d$. Then, $\mathcal{K}_d$ behaves as [37]

$$\mathcal{K}_d(\omega = \omega_{ad}) \to 0 \quad \text{and} \quad \mathcal{K}_d(\omega = \omega_{gd}) \to \infty. \tag{39}$$

At the anti-resonance frequency ω_{ad}, the mean fluid velocity tends to zero when the system is excited by a finite pressure gradient. Physically, this implies that the internal motions of the fluid-film system compensate. At the resonance frequency ω_{gd}, the mean fluid velocity takes large values when the system responds to a finite pressure gradient.

It then follows that the magnitude and phase of the effective density ρ_d tend to

$$|\rho_d(\omega = \omega_{ad})| \to \infty \quad \text{and} \quad |\rho_d(\omega = \omega_{gd})| \to 0, \tag{40}$$

$$\theta_{\rho_d}(\omega = \omega_{ad}) = -\frac{\pi}{2} \quad \text{and} \quad \theta_{\rho_d}(\omega = \omega_{gd}) \to -\frac{\pi}{2}. \tag{41}$$

It is clear that in the frequency band $(\omega_{ad}, \omega_{gd})$, the magnitude of ρ_d is a decreasing function of frequency, while its phase reflects that the movement of the equivalent fluid is in the opposite direction to the driving force, i.e. θ_{ρ_d} tends to

$$\theta_{\rho_d}(\omega_{ad} < \omega < \omega_{gd}) \to -\pi. \tag{42}$$

14

Consequently, the real part of ρ_d is negative in the frequency band $(\omega_{ad}, \omega_{gd})$, i.e $\Re(\rho_d(\omega_{ad} < \omega < \omega_{gd})) < 0$.

Gathering the previous results, the limiting behavior of the effective permeability and density of the permeable lossy metamaterial is identified. For negligible elastic effects, the former behaves as

$$\mathcal{K}(\omega \ll \omega_v) \to \phi_b \mathcal{K}_{b0} + \phi_d \mathcal{K}_{d0} = \mathcal{K}_0 \quad \text{and} \quad \mathcal{K}(\omega \gg \omega_v) \to -\mathrm{j}\phi\frac{\delta_v^2}{\alpha_\infty}, \tag{43}$$

where $\alpha_\infty = \phi/(\phi_b \alpha_{\infty b}^{-1} + \phi_d \alpha_{\infty d}^{-1})$ is the overall tortuosity of the metamaterial and $\phi = \phi_b + \phi_d$. The Biot frequency ω_v is implicitly defined through

$$\phi_b \mathcal{V}_b(\omega_v) + \phi_d \mathcal{V}_d(\omega_v) = \phi_b \mathcal{I}_b(\omega_v) + \phi_d \mathcal{I}_d(\omega_v) \quad \text{with} \quad \phi_d \mathcal{E}_d \to 0, \tag{44}$$

and can be well estimated by $\omega_v = \phi\nu/\mathcal{K}_0\alpha_\infty$.

The magnitude and phase of the dynamic density ρ tend to

$$|\rho(\omega \ll \omega_v)| \to \rho_0\frac{\delta_v^2}{\mathcal{K}_0} \quad \text{and} \quad |\rho(\omega \gg \omega_v)| \to \frac{\rho_0\alpha_\infty}{\phi}, \tag{45}$$

$$\theta_\rho(\omega \ll \omega_v) = -\frac{\pi}{2} \quad \text{and} \quad \theta_\rho(\omega \gg \omega_v) \to 0. \tag{46}$$

The locally resonant behavior of the perme-elastic domain affects the effective permeability and density of the permeable lossy metamaterial. The elasto-inertial characteristic frequencies ω_a and ω_g are implicitly defined through

$$\phi_d \mathcal{E}_d(\omega_{ei}) = \phi_b \mathcal{I}_b(\omega_{ei}) + \phi_d \mathcal{I}_d(\omega_{ei}) \quad \text{with} \quad (\phi_b \mathcal{V}_b(\omega_{ei}) + \phi_d \mathcal{V}_d(\omega_{ei})) \to 0, \tag{47}$$

where ω_{ei} equals to either ω_a or ω_g.

At the anti-resonance frequency ω_a (respectively resonance frequency ω_g), one has that $\mathcal{K}(\omega_a) \to 0$ (respectively $\mathcal{K}(\omega_g) \to \infty$). It is worth highlighting that ω_a is determined by the elasticity and inertia of the films and the fluid saturating Ω_{bf} and Ω_{df}. The relationship between this anti-resonance frequency and that of the permeo-elastic domain ω_{ad} is shown to be $\omega_a \geq \omega_{ad}$, with the equality being observed when $\mathcal{I}_b \to 0$. On the other hand, since $\mathcal{K}_d(\omega_{gd}) \to \infty$, the overall permeability also tends to ∞ at the resonance frequency $\omega_g = \omega_{gd}$. Hence, ω_g does not depend on fluid flow in Ω_{bf}. These results lead to the following behavior of the effective density

$$|\rho(\omega = \omega_a)| \to \infty \quad \text{and} \quad |\rho(\omega = \omega_g)| \to 0, \tag{48}$$

15

$$\theta_\rho(\omega = \omega_a) = -\frac{\pi}{2} \quad \text{and} \quad \theta_\rho(\omega = \omega_g) \to -\frac{\pi}{2}. \tag{49}$$

Note also that in the frequency band $\Delta_d = (\omega_a, \omega_g)$, the magnitude of ρ is a decreasing function of frequency, while the phase of the effective density tends to

$$\theta_\rho(\omega_a < \omega < \omega_g) \to -\pi. \tag{50}$$

This shows that the real part of ρ is negative in this frequency range and means that the movement of the equivalent fluid is in the opposite direction to the driving force.

At this point, some remarks are pertinent: i) despite the fact that the flow in the fluid network Ω_{df} is uncoupled from that in Ω_{bf}, the latter still affects the overall anti-resonance frequency of the permeable lossy metamaterial. This enables the tuning of ω_a by, for example, modifying the pore morphology Ω_{bf}; and thereby the tuning of the band where $\Re(\rho) < 0$, and ii) the small but non negligible viscous dissipation leads to damped resonances and, as a consequence, removing the singularities of the effective parameters, while the excess of dissipation can over damp the resonances.

B. Effective dynamic compressibility

Consider frequencies much smaller than the thermal characteristic frequencies $\omega_{t\iota}$, defined through $\mathcal{H}_\iota(\omega_{t\iota}) = \mathcal{S}_\iota(\omega_{t\iota})$ and estimated as $\omega_{t\iota} = \kappa/\rho_0 c_p \Theta_{0\iota}$, where $\Theta_{0\iota}$ is the static thermal permeability of the pore fluid network $\Omega_{\iota f}$ (with $\iota = d, b$). At the leading order, $\mathcal{H}_\iota(\omega \ll \omega_{t\iota}) \to \frac{\gamma-1}{\gamma} \frac{\omega}{\omega_{t\iota}}$ and $\mathcal{S}_\iota(\omega \ll \omega_{t\iota}) \to 0$. Hence, $\Theta_\iota(\omega \ll \omega_{t\iota}) \to \Theta_\iota(\omega = 0) = \Theta_{0\iota}$. For $\omega \gg \omega_{t\iota}$, the leading-order limiting values are $\mathcal{H}_\iota(\omega \gg \omega_{t\iota}) \to 0$ and $\mathcal{S}_\iota(\omega \gg \omega_{t\iota}) \to (\gamma - 1)/\gamma$, i.e. $\Theta_\iota(\omega \gg \omega_{t\iota}) \to -\mathrm{j}\delta_t^2$, where the thermal boundary layer thickness is $\delta_t = \sqrt{\kappa/\rho_0 c_p \omega}$. Consequently, the effective compressibilities C_d and C_b behave classically, i.e.

$$\mathsf{C}_\iota(\omega \ll \omega_{t\iota}) \to \frac{1}{P_0}\left(1 - \frac{\gamma-1}{\gamma}\frac{\mathrm{j}\omega}{\omega_{t\iota}}\right) \quad \text{and} \quad \mathsf{C}_\iota(\omega \gg \omega_{t\iota}) \to \frac{1}{\gamma P_0}. \tag{51}$$

The magnitude and phase of the effective compressibilities then tend to

$$|\mathsf{C}_\iota(\omega \ll \omega_{t\iota})| \to \frac{1}{P_0}\sqrt{1 + \left[\frac{\gamma-1}{\gamma}\frac{\omega}{\omega_{t\iota}}\right]^2} \quad \text{and} \quad |\mathsf{C}_\iota(\omega \gg \omega_{t\iota})| \to \frac{1}{\gamma P_0}, \tag{52}$$

$$\theta_{\mathsf{C}_\iota}(\omega \to 0) \to 0 \quad \text{and} \quad \theta_{\mathsf{C}_\iota}(\omega \gg \omega_{t\iota}) \to 0. \tag{53}$$

16

Using Eq. (C.20), one then obtains that (with $\omega_t^{\min} = \min(\omega_{tb}, \omega_{td})$ and $\omega_t^{\max} = \max(\omega_{tb}, \omega_{td})$)

$$\mathsf{C}(\omega \ll \omega_t^{\min}) = \left[\frac{\phi_b}{P_0} + \phi_b \frac{2}{\mathcal{L}} \frac{\mathcal{Y}_r^{\Im}}{\omega} + \frac{\phi_d}{P_0}\right] - \mathrm{j}\left[\frac{\phi_b}{P_0}\frac{\gamma-1}{\gamma}\frac{\omega}{\omega_{tb}} + \phi_b\frac{2}{\mathcal{L}}\frac{\mathcal{Y}_r^{\Re}}{\omega} + \frac{\phi_d}{P_0}\frac{\gamma-1}{\gamma}\frac{\omega}{\omega_{td}}\right], \quad (54)$$

$$\mathsf{C}(\omega \gg \omega_t^{\max}) = \left[\frac{\phi_b}{\gamma P_0} + \phi_b \frac{2}{\mathcal{L}} \frac{\mathcal{Y}_r^{\Im}}{\omega} + \frac{\phi_d}{\gamma P_0}\right] - \mathrm{j}\left[\phi_b\frac{2}{\mathcal{L}}\frac{\mathcal{Y}_r^{\Re}}{\omega}\right], \quad (55)$$

where $\mathcal{Y}_r^{\Re} = \Re(\mathcal{Y}_r)$ and $\mathcal{Y}_r^{\Im} = \Im(\mathcal{Y}_r)$.

To gain further insight, it is convenient to use a particular expression for the admittance of the resonator. The features to be identified are, however, shared by other types of acoustic resonators. Considering a quarter-wavelength resonator, the effective admittance of which is given by Eq. (B.1), one has that $\mathcal{Y}_r \approx \mathrm{j}\omega\mathsf{C}_{\tilde{r}}d_r$ for $|k_{cr}d_r| \ll 1$, where k_{cr} and $\mathsf{C}_{\tilde{r}}$ are, respectively, the effective wave number and compressibility of the fluid saturating the quarter-wavelength resonator of depth d_r. The effective compressibility $\mathsf{C}_{\tilde{r}}$ takes the following leading-order limiting values: $\mathsf{C}_{\tilde{r}}(\omega \ll \omega_{tr}) = 1/P_0$ and $\mathsf{C}_{\tilde{r}}(\omega \gg \omega_{tr}) = 1/\gamma P_0$. Then, the term $2\phi_b\mathcal{Y}_r^{\Im}/\mathcal{L}\omega$, becomes either ϕ_r/P_0 or $\phi_r/\gamma P_0$ for $\omega \ll \omega_{tr}$ or $\omega \gg \omega_{tr}$, respectively. Note that $\phi_r = \Omega_{rf}/\Omega$.

The low frequency asymptotic value of the overall normalized effective compressibility is therefore given by

$$P_0\mathsf{C}(\omega \to 0) = \Phi - \frac{\gamma-1}{\gamma}\frac{\mathrm{j}\omega}{\omega_t} \quad \text{i.e.} \quad \mathsf{C}(\omega = 0) = \frac{\Phi}{P_0} \quad (56)$$

where $\Phi = \phi_b + \phi_r + \phi_d$ is the total porosity of the metamaterial and the apparent thermal characteristic frequency ω_t is defined through $\omega_t^{-1} \approx \phi_b/\omega_{tb} + \phi_d/\omega_{td}$. This is an approximated expression because a small contribution of a visco-elastic frequency coming from the loading resonator has been omitted. Note also that the same result applies to a metamaterial whose REV features a Helmholtz instead of a quarter-wavelength resonator but with $\phi_r \to \phi_n + \phi_a$, where $\phi_n = \Omega_n/\Omega$ and $\phi_a = \Omega_a/\Omega$ are the volume fractions occupied by the neck and cavity of the resonator, respectively.

Then, the magnitude and phase of the effective compressibility (with $\omega/\omega_t \ll 1$) tends to

$$|\mathsf{C}(\omega \to 0)| \to \frac{\Phi}{P_0}\sqrt{1 + \left[\frac{\gamma-1}{\gamma\Phi}\frac{\omega}{\omega_t}\right]^2} \approx \frac{\Phi}{P_0} \quad \text{and} \quad \theta_{\mathsf{C}}(\omega \to 0) \to 0. \quad (57)$$

Since $0 \leq \mathcal{S}_\iota \leq (\gamma-1)/\gamma$ (with $\iota = b, d$), Eq. (C.20) shows that the real part of the effective compressibility is positive, provided that $\mathcal{Y}_r^{\Im} \geq 0$. This can also be seen from

17

Eqs. (54) and (55). However, at the resonance frequency f_r of a lossless acoustic resonator, the compressibility diverges [34]. Consequently, the magnitude and phase of the effective compressibility at ω_r tend to

$$|\mathsf{C}(\omega = \omega_r)| \to \infty, \quad \text{and} \quad \theta_{\mathsf{C}}(\omega = \omega_r) \to -\frac{\pi}{2}. \tag{58}$$

The real part of the effective compressibility can be negative, i.e. $\Re(\mathsf{C}) < 0$. With reference to Eq. (C.20), this occurs in the frequency band where the following inequality is satisfied

$$\mathcal{Y}_r^{\Im} < -\frac{\omega}{P_0} \frac{\Omega}{\Gamma_{rf}} \left(\phi_b(1 - \mathcal{S}_b) + \phi_d(1 - \mathcal{S}_d) \right). \tag{59}$$

It is clear that $\Re(\mathsf{C}) < 0$ is only possible if $\mathcal{Y}_r^{\Im} < 0$. For the case of a lossless quarter-wavelength resonator, one has the following inequality

$$\tan(\xi) < -\phi^\star \xi \quad \text{with} \quad \phi^\star = \frac{\phi_b/g_b + \phi_d/g_d}{\phi_r/\gamma}, \tag{60}$$

where Eq. (B.1) has been used, $\xi = \pi \omega / 2\omega_r$, and g_d and g_b can take values of 1 or γ, depending on whether sound propagation in the respective equivalent fluid is isothermal or adiabatic. Note that a necessary but not sufficient condition to satisfy (60) is $1 \leq \omega/\omega_r < 2$.

The inequality (60) is transcendental and shows that, despite the fact that the two fluid networks are unconnected and therefore the waves that propagate in them do no interact, there is still an influence of the fluid network Ω_{df}, through its associated porosity, on the atypical behavior of the effective compressibility. In practice, this means that the second porosity can be used to make the frequency band where $\Re(\mathsf{C}) < 0$ narrower. However, the fluid network Ω_{df} does not modify the resonance frequency ω_r at which $|\mathsf{C}| \to \infty$.

To estimate the frequency band $\Delta_b = (\omega_r, \omega_{r\star})$ where $\Re(\mathsf{C}) < 0$, an approximation of the left-hand side term of Eq. (60) is used, i.e.

$$\frac{\omega_* - 2}{1 - \omega_*^2} = \phi^\star \omega_* \quad \text{with} \quad \omega_* = \frac{\omega}{\omega_r}. \tag{61}$$

The solution of this equation leads to

$$\frac{\omega_{r\star}}{\omega_r} = \mathfrak{z} + \frac{1}{3\mathfrak{z}} \frac{\phi^\star - 1}{\phi^\star}, \tag{62}$$

$$\mathfrak{z} = \left(\frac{1}{\phi^\star} \right)^{1/3} \left[1 + \sqrt{1 - \frac{(\phi^\star - 1)^3}{27\phi^\star}} \right]^{1/3}. \tag{63}$$

18

Focusing on the first resonance, assuming adiabatic sound propagation in Ω_{bf}, Ω_{df} and Ω_{rf} (i.e. the frequency is much higher than any thermal characteristic frequency and therefore $g_b = g_d = \gamma$), and recalling that for any frequency $\omega_{r\star}/\omega_r < 2$ otherwise the imaginary part of the admittance cannot take negative values, it can be shown from Eqs. (63) and (62) that $\omega_{r\star}/\omega_r$ is a decreasing function of $\phi^\star$ that takes the limiting values $\omega_{r\star}/\omega_r \to 2$ for $\phi^\star \ll 1$ and $\omega_{r\star}/\omega_r \to 1$ for $\phi^\star \gg 1$. This reflects that a larger (respectively smaller) fluid-saturated volume occupied by the quarter-wavelength resonator maximizes (respectively minimizes) the bandwidth of Δ_b.

For the case of a permeable lossy metamaterial with one Helmholtz resonator per REV and considering a 'lumped' parameter approximation obtained by i) expanding the effective admittance Eq. (B.2) for $|k_{ca}h_a| \ll 1$ and $|k_{cn}l_n| \ll 1$, and ii) considering adiabatic sound propagation everywhere (i.e. the frequency is much higher than any thermal characteristic frequency and therefore $g_a = g_b = g_d = \gamma$); the ratio $\omega_{r\star}/\omega_r$ takes a simple form, i.e.

$$\frac{\omega_{r\star}}{\omega_r} = \sqrt{1 + \frac{\phi_a}{\phi_b + \phi_d}}. \tag{64}$$

The magnitude and phase of the effective compressibility at the anti-resonance frequency $\omega_{r\star}$ tend to

$$|\mathsf{C}(\omega = \omega_{r\star})| \to 0 \quad \text{and} \quad \theta_\mathsf{C}(\omega = \omega_{r\star}) \to -\frac{\pi}{2}. \tag{65}$$

Furthermore, even though the heat transfer in the fluid network Ω_{bf} is uncoupled from that in Ω_{df}, the heat transfer in the latter affects the frequency band where $\Re(\mathsf{C}(\omega)) < 0$. The existence of the additional pore network makes this band narrower and the phase of the material's effective compressibility approaches

$$\theta_\mathsf{C}(\omega_r < \omega < \omega_{r\star}) \to -\pi. \tag{66}$$

C. Effective speed of sound and wave number

Eq. (34) shows that $|c(\omega)| \to 0$ if $|\mathcal{K}| = 0$ or $|\mathsf{C}| \to \infty$. These conditions are not satisfied in conventional porous materials [42], multiscale permeable media [73, 74, 76–79], or porous composites [82, 83]. As an example, for conventional porous materials and considering leading-order terms: $c_0\sqrt{\omega\mathcal{K}_0/\phi\gamma\nu} \le |c| \le c_0/\sqrt{\alpha_\infty}$ while the phase of the effective speed of sound varies from $\pi/4$ in viscosity-dominated flow regime down to 0 in inertia-dominated

flow regime. Consequently, the magnitude of the wave number take the following values $k_0\sqrt{\phi\gamma\nu/\omega\mathcal{K}_0} \leq |k_c| \leq k_0\sqrt{\alpha_\infty}$, where $k_0 = \omega/c_0$ is the wave number in air. This classical behavior is not totally shared by permeable lossy metamaterials.

As follows from the previous subsections, the magnitude and phase of the effective speed of sound take the following values for low and high frequencies

$$|c(\omega \ll \omega_v)| \to c_0\sqrt{\frac{\omega\mathcal{K}_0}{\Phi\gamma\nu}} \quad \text{and} \quad |c(\omega \gg \omega_v)| \to \frac{c_0}{\sqrt{\alpha_\infty}}, \tag{67}$$

$$\theta_c(\omega \ll \omega_v) \to \frac{\pi}{4} \quad \text{and} \quad \theta_c(\omega \gg \omega_v) \to 0. \tag{68}$$

Since $|k_c(\omega)| = \omega/|c(\omega)|$ and $\theta_k(\omega) = -\theta_c(\omega)$, it is direct to obtain the limiting values of the magnitude and phase of the wave number. Hence, for the sake of brevity, these will not be quoted in what follows.

Recalling that for elasto-inertial flow, the effective permeability at ω_a tends to zero, while at ω_g it tends to ∞ [see also Eq. (48)]; and further assuming adiabatic sound propagation in both pore fluid networks, one obtains that

$$|c(\omega_a)| \to 0 \quad \text{and} \quad |c(\omega_g)| \to \infty, \tag{69}$$

$$\theta_c(\omega_a) \to \frac{\pi}{4} \quad \text{and} \quad \theta_c(\omega_g) \to \frac{\pi}{4}, \tag{70}$$

while in the band (ω_a, ω_g) the phase of the effective speed of sound tends to

$$\theta_c(\omega_a < \omega < \omega_g) \to \frac{\pi}{2}. \tag{71}$$

Thus, the real part of the effective speed of sound (or phase velocity) tends to zero while the imaginary part increases significantly. This means that no propagating waves are supported in Δ_d and a bandgap is developed in this frequency range.

On the other hand, for inertia-dominated flow, the presence of resonators also affect the effective sound speed. On the boundaries ω_r and $\omega_{r\star}$ of the frequency range where $\Re(\mathsf{C}) < 0$, one has that

$$|c(\omega_r)| \to 0 \quad \text{and} \quad |c(\omega_{r\star})| \to \infty, \tag{72}$$

$$\theta_c(\omega_r) \to \frac{\pi}{4} \quad \text{and} \quad \theta_c(\omega_{r\star}) \to \frac{\pi}{4}. \tag{73}$$

In the frequency band $(\omega_r, \omega_{r\star})$, the phase of the effective speed of sound tends to

$$\theta_c(\omega_r < \omega < \omega_{r\star}) \to \frac{\pi}{2}, \tag{74}$$

and $\Re(c) \to 0$. This means that a second bandgap is developed in this frequency range.

In summary, two band gaps are predicted due to two different resonance mechanisms, i.e. acoustic resonance and fluid-film resonance, when the two atypical bands do not overlap. In both bands, the real part of the speed of sound (or phase velocity) tends to zero while the attenuation coefficient, defined as $-\Im(k_c)$, takes large values.

Up to now, it has been tacitly assumed that the two atypical bands do not overlap. However, the overlap is not prohibited and this leads to behavior typical for double negative metamaterials [6–10, 12, 14].

In the frequency band, denoted as Δ, where $\Delta_d = (\omega_a, \omega_g)$ and $\Delta_b = (\omega_r, \omega_{r\star})$ overlap, the phase of the effective speed of sound tends to

$$\theta_c(\omega \in \Delta) \to \pi. \tag{75}$$

This means that the phase velocity is negative in Δ, leading to a negative real part of the refraction index in Δ. Negative phase velocity is a remarkable feature and its prediction highlights the need to properly account for losses in the modeling. Ignoring the losses, accounted for by the imaginary parts of such effective parameters, a positive phase velocity in Δ may be predicted since both $\Re(\rho)$ and $\Re(C)$ are negative in this band. It should be emphasized that a negative phase velocity means that the propagating wave is regressive. However, it is stressed that the attenuation coefficient is positive and the wave amplitude is decreasing for frequencies in Δ, which is consistent with the fact that no gain is expected in a passive material.

Interesting cases arise when elasto-inertial characteristic frequencies are matched. When the dipolar anti-resonance of the fluid-film system coincides with the monopolar resonance of the acoustic resonator, i.e. $\omega_a = \omega_r$, the magnitude and phase of the effective speed of sound tend, respectively, to $|c| \to 0$ and $\theta_c \to \pi/2$. If the anti resonance ω_a coincides with the upper boundary of bandgap $\omega_{r\star}$, then $\theta_c \to \pi/2$ and a local minimum in $|c|$ is expected due to the usually larger magnitude of ρ in comparison with that of C. If two resonance frequencies coincide, i.e. $\omega_g = \omega_r$, $|c|$ is expected to have a local maximum and θ_c to tend to $\pi/2$. In addition, $|c| \to \infty$ and $\theta_c \to \pi/2$ at $\omega = \omega_g = \omega_{r\star}$.

The limiting cases considered so far are best approached when losses are small. Due to the presence of losses, these limiting values are not reached and the phase behavior is smoothed. The latter can also be exploited to induce anomalous acoustic wave propagation

in narrow frequency bands. These phenomena are investigated in the subsequent parts.

IV. HYBRID MODEL

The modelling of permeable lossy metamaterials requires the calculations of their effective parameters $\mathcal{K}$ and C, which, in turn, requires those of $\mathcal{K}_d$, $\mathcal{K}_b$, C_b, C_r, and C_d. These are dependent on the saturating fluid, mechanical parameters of the films, and geometry of the microstructure.

Figure 2 shows the microstucture of a permeable lossy metamaterial, to be used in examples, comprising a slit-like channel loaded with an acoustic resonator, a permeo-elastic channel, and a solid frame. The REV is a parallelepiped with sides l_t, l_w, and l_h. The width of the permeo-elastic channel is w_d, while the width w_s of the solid walls that decouple the domains Ω_{bf} and Ω_{df} is equal to their height h_s. The width of the slit-like channel loaded with the Helmholtz resonator is $h_b = 2h$. The Helmholtz resonator has a cylindrical cavity, of radius r_a and depth h_a, with an in-built cylindrical neck with radius r_n and length l_n. The height of the gap that connects the front and back fluid-saturated parts of the permeo-elastic channel is h_g. The height and depth of the bar one of the edges of the film is clamped onto are h_q and d_q, respectively. The dimensions of the rectangular film are h_m and $w_m = w_d$. The geometry of the microstructure of other materials, described and used for comparison purposes in the the next section, are also shown in Figure 2.

The dynamic visco-inertial permeability $\mathcal{K}_b$ and dynamic thermal permeability Θ_b of air in the slit side-loaded by resonators are given by

$$\mathcal{K}_b(\omega) = \chi(h, \delta_v) \quad \text{and} \quad \Theta_b(\omega) = \chi(h, \delta_t), \tag{76}$$

where

$$\chi(x, \delta) = -\mathrm{j}\delta^2 \left(1 - \frac{\tanh\left(\sqrt{\mathrm{j}}x\delta^{-1}\right)}{\sqrt{\mathrm{j}}x\delta^{-1}}\right). \tag{77}$$

Then, the compressibility of air in the slit side-loaded by resonators, i.e. C_b, is calculated by inserting Eq. (76) into (27), while C_r is given by Eq. (28) with $\mathcal{Y}_r$ being given by Eq. (B.2). Viscothermal losses in the neck and cavity of the resonator are accounted for via the complex-valued frequency-dependent wave number and characteristic impedance. These are calculated (with $\beta = n, a$) as $k_{c\beta} = \omega\sqrt{\eta\mathsf{C}_\beta/\mathrm{j}\omega\mathcal{K}_\beta}$ and $Z_{c\beta} = \omega\eta/\mathrm{j}\omega\mathcal{K}_\beta k_{c\beta}$. Here $\mathcal{K}_\beta$ is
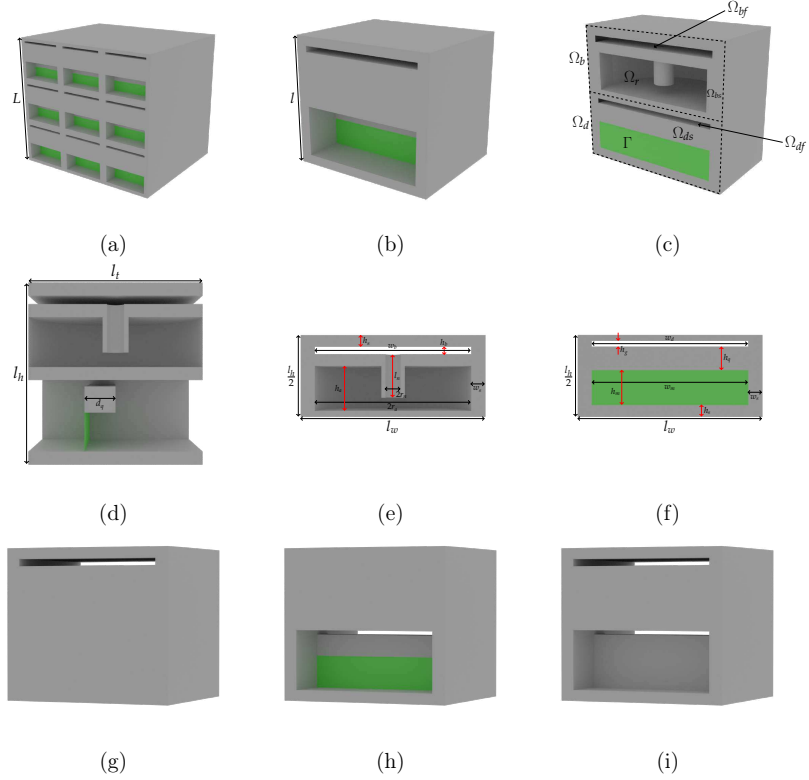
FIG. 2: Geometry of a permeable lossy metamaterial. (a) 3D macroscopic medium. (b) 3D REV. (c) and (d) cutaway views of the 3D REV. (e) and (f) Geometrical parameters of the domains Ω_b and Ω_d. (g) 3D REV of a single porosity material (SPM). (h) 3D REV of a permeo-elastic material (PEM). (i) 3D REV of a double porosity material (DPM).

calculated with the well known model proposed in [45, 48], i.e.

$$\mathcal{K}_\beta(\omega) = \mathcal{F}(\mathcal{K}_{0\beta}, \omega_{v\beta}, M_{v\beta}), \tag{78}$$

with $\mathcal{K}_{0\beta} = r_\beta^2/8$, $\omega_{v\beta} = 8\nu/r_\beta^2$, $M_{v\beta} = 1$, and

$$\mathcal{F}(\mathcal{F}_0, \varpi, \mathcal{M}) = \mathcal{F}_0 \left(\frac{\mathrm{j}\omega}{\varpi} + \sqrt{1 + \frac{\mathrm{j}\omega}{\varpi} \frac{\mathcal{M}}{2}} \right)^{-1}. \tag{79}$$

The effective compressibilities C_β are calculated by replacing b by β in Eq. (27) and the

respective dynamic thermal permeabilities are given by $\Theta_\beta = \mathcal{F}(\Theta_{0\beta}, \omega_{t\beta}, M_{t\beta})$ with $\Theta_{0\beta} = r_\beta^2/8$, $\omega_{t\beta} = 8\kappa/\rho_0 c_p r_\beta^2$, and $M_{t\beta} = 1$.

Due to both the complex geometry of the permeo-elastic channel and the strong fluid-film interaction, the dynamic visco-elasto-inertial permeability $\mathcal{K}_d$ is calculated from the numerical solution of the boundary-value problem detailed in § A 3 c and using Eq. (31). The calculations of $\mathcal{K}_d$ are performed using the finite element method, as detailed in [36, 37]. The effective compressibility C_d is obtained by substituting the expression for the dynamic thermal permeability Θ_d into Eq. (29). This dynamic thermal permeability is calculated as

$$\Theta_d(\omega) = \mathcal{F}(\Theta_{0d}, \omega_{td}, M_{td}), \tag{80}$$

where the thermal characteristic frequency, shape factor, and characteristic length are $\omega_{td} = \kappa/\rho_0 c_p \Theta_{0d}$, $M_{td} = 8\Theta_{0d}/\Lambda_{td}^2$, and Λ_{td}, respectively. These parameters are calculated using the finite element method, as discussed in detail in [63].

V. ILLUSTRATING EXAMPLES

The hybrid model is used in this section to exemplify the atypical acoustical properties of a permeble lossy metamaterial, which, for the sake of brevity, will be referred to as PLM.

The microstructure of the PLM is shown in Fig. 2. The REV is a parallelepiped with sides $l_t = 25$ mm, $l_w = w_d + 2w_s$, and $l_h = 4h_s + h_b + h_a + h_g + h_q + h_m$, where $w_d = 20$ mm is the width of the permeo-elastic channel, $w_s = h_s = 1.5$ mm is the width of the solid walls, $h_b = 2h = 3$ mm is the width of the slit-like channel side-loaded with the Helmholtz resonator, $h_a = 27$ mm is the depth of the cylindrical cavity of the Helmholtz resonator, and $h_g = 1$ mm is the height of the gap that connects the front and back fluid-saturated domains of the permeo-elastic channel, $h_q = d_q = 4$ mm is the height of the bar one of the edges of the film is clamped onto, and the dimensions of the rectangular film are $h_m = 10$ mm and $w_m = w_d = 20$ mm. The film thickness is $t = 76$ μm. The other parameters of the Helmholtz resonator are the radius of its cylindrical cavity $r_a = 7$ mm, the length of its neck $l_n = 7$ mm, and the diameter of its neck $2r_n = 3$ mm. The mechanical parameters of the films are those of Mylar, i.e. $E = 2.25$ GPa, $\rho_s = 1390$ kg/m³, and $\nu = 0.38$. The films are pre-stressed with a uniform tension per unit thickness $\mathcal{T} = 1$ N/m. Normal pressure and temperature condition is considered.

The large number of geometrical and mechanical parameters involved provides a plethora of possibilities to tailor the acoustic behavior of the PLM. However, in what follows, the parameters quoted above are kept constant unless otherwise explicitly stated.

A.   Example 1 – Non overlapping atypical frequency bands

Figure 3a–d show a comparison between the dynamic density and compressibility of the PLM and those of i) a double porosity material (DPM) with weakly contrasted permeabilities and a REV comprising a solid part, a slit-like channel (without the loading Helmholtz resonators), and ii) a permeo-elastic channel but with perfectly rigid instead of elastic films [see Figures 2(i) and 2(h), respectively]. The characteristic frequencies of interest of the PLM have been determined from their definition. These are $f_v = 4$ Hz, $f_a = 610$ Hz, $f_g = 677$ Hz, $f_r = 801$ Hz, and $f_{r\star} = 978$ Hz.

As predicted through the analysis presented in § III, at frequencies much lower than f_v, the dynamic density of the PLM and DPM coincides, while their effective compressibilities differ. For the dynamic density, this is because the films behave as perfectly rigid while for C this is due to the fact that the whole fluid-filled volume of the Helmholtz resonators affects the dynamic compressibility of the PLM. As the frequency increases, the differences in the effective parameters of the PLM and DPM become apparent. At the anti-resonance frequency f_a, the magnitude of the dynamic density of the PLM takes its smallest value while at the resonance frequency f_g is maximum, although not infinite due to the small but non-negligible viscous dissipation. Within the atypical band $\tilde{\Delta}_d = (f_a, f_g)$, the phase of ρ approaches $-\pi$ and consequently $\mathrm{Re}(\rho) < 0$. This is because in $\tilde{\Delta}_d$ the elasticity of the films dominates over the inertia of the whole fluid-film system, i.e. $\phi_d \mathcal{E}_d > [\phi_b \mathcal{I}_b + \phi_d \mathcal{I}_d]$ (see also Eq. (C.12)). Note also that the value $\theta_\rho = -\pi$ is not achieved due to viscous dissipation, which also makes the transitions between the atypical and classical behavior smoother. This is typical for a band structure of lossy metamaterials. The classical behavior is recovered for frequencies over f_g, provided that no higher-order modes of the fluid-film system are observed.

The magnitude of the effective compressibility of the PLM takes its extreme values at the boundaries of the atypical band $\tilde{\Delta}_b = (f_r, f_{r\star})$. As discussed in § III, at f_r and $f_{r\star}$ the phase of the effective compressibility approaches $-\pi/2$, while in between them it tends to $-\pi$ in

25

absence of dissipation. The larger value of θ_C, shown in Fig. 3(d), is attributed to the viscous dissipation in the neck of the Helmholtz resonators, which also explains the regularization of $|C|$ at the resonance frequency f_r. It is recalled that $\Re(C) < 0$ in $\tilde{\Delta}_b$. Contrarily to the atypical band induced by the fluid-film interaction in Ω_{df}, in this case it is the effective inertia of the fluid in the resonator that dominates over the elasticity of the whole fluid system, which is consistent with the fact that the lowest frequency in $\tilde{\Delta}_b$ corresponds to a resonance frequency, instead of an anti-resonance frequency as it is the case in $\tilde{\Delta}_d$.

For $f \ll f_v$, the phase velocity as well as the magnitude and phase of c in the PLM behave classically, which it is also the case for the wave number [see Fig.3(e)–(h)]. For $f_v \ll f \ll f_g$, anomalous dispersion appears since the phase velocity in the PLM decreases. This is in contrast with the behavior of DPM [cf. black continuous and dashed gray lines in Fig. 3e]. While the real part of the wave number (i.e. the phase constant) of the PLM and DPM increases linearly with frequency for $f_v \ll f \ll f_g$, the slope of the phase constant of the PLM is more pronounced. This is consistent with its slower phase velocity in comparison with that in DPM. Such increase, however, becomes non linear as $f \to f_a$ due to the influence of the elasticity of the films on the acoustic behavior. Moreover, the phase constant and attenuation coefficient at f_a take large values.

Within the atypical band $\tilde{\Delta}_d$, the phase constant rapidly approaches its minimum value, while the attenuation coefficient decreases down to its minimum value at the frequency at which the phase velocity takes its largest (supersonic) value, i.e. at f_g. For $f_g < f < f_r$, the phase velocity decreases while both the phase constant and attenuation coefficient increase until reaching a local maximum, just below and above f_r, respectively. On the other hand, the phase velocity in $\tilde{\Delta}_b$ decreases until reaching a plateau region to then increase up to its maximum value within the atypical band. Consistently, the phase constant follows the inverse trend while the attenuation coefficient is a decreasing function of frequency in $\tilde{\Delta}_b$. Since the phase of the effective speed of sound does not reach $\pi/2$, the atypical band can only be considered as a quasi or pseudo band gap. This highlights the fact that excess of dissipation, in this case occurring in the neck of the resonator, can prevent the existence of a true band gap. It is emphasized, however, that the attenuation coefficient in $\tilde{\Delta}_b$ is still significant, which reflects the high attenuation of sound within such band. On the other hand, this example shows that the phase of the effective speed of sound tends to $\pi/4$ at $f_{r\star}$ and the phase velocity is close to c_0. This means that a diffusive wave travels through the

26

PLM at the speed of sound in lossless air. In the long-wavelength regime, such a behavior is not possible to observe in conventional porous material. Moreover, for frequencies over $f_{r\star}$, the phase velocity takes supersonic values due to the small magnitude of the effective compressibility.

In summary, the results shown in Fig. 3 confirm the theoretical analysis presented in § III and are characteristics of a PLM in which the atypical bands $\tilde{\Delta}_b$ and $\tilde{\Delta}_d$ are neither overlapping nor adjacent. In what follows, some of the geometrical parameters of the Helmholtz resonator of PLM are varied to exemplify both the overlapping of the atypical bands and cases where the elasto-inertial characteristic frequencies are matched.

B. Example 2 – Overlapping atypical frequency bands

In this example, the neck length and radius of the cavity of the Helmholtz resonator are $l_n = 9$ mm and $r_a = 9$ mm, respectively. For this PLM, the atypical bands overlap and are given by $\tilde{\Delta}_b = (f_r, f_{r\star}) = (555, 746)$ Hz and $\tilde{\Delta}_b = (f_a, f_g) = (610, 677)$ Hz. Figure 4 shows the same effective parameters as those displayed in Fig. 3.

In the viscosity-dominated flow regime, i.e. for $f \ll f_v$, the effective speed of sound and wave number behave as in the example 1. For $f_r < f < f_a$, the real part of the effective density is positive, the real part of the effective compressibility is negative, the phase velocity is slow, the phase constant is a decreasing function of frequency, and the attenuation coefficient exhibits peaks just over f_r and at f_a, with the former peak being slightly merged with the latter one since, in this example, the difference between f_a and f_r is only 55 Hz.

In the region of double negativity, the phase of the effective speed of sound approaches π, which reflects a negative phase velocity and a negative phase constant. This is accompanied by a pronounced decrease in the attenuation coefficient. Physically, in the region of double negativity, regressive waves propagate in the effective medium. The physical origin of this peculiar behavior is the dominance of the elastic effects of the films in the permeo-elastic channel and that of the inertia of the effective fluid saturating the neck of the resonator that loads the pore fluid network Ω_{bf}. The peculiar behavior is not only seen in the region of double negativity but also just below/above the lower/upper band-edge frequencies and when the atypical bands are adjacent. This is due to the presence of dissipation, which smooths

the phase transition. Hence, regressive waves are not exclusive to the double negativity region, as it can be seen by close inspection of Fig. 4e and in other examples below.

In between f_g and $f_{r\star}$, a local maximum/minimum in the attenuation coefficient/phase velocity is seen. This is accompanied by a close to zero phase constant. In the frequency region, where in this example only $\Re(\mathsf{C})$ is negative, θ_c decreases from $\pi/2$ to $\pi/4$, while the phase velocity increases over c_0. In this example, the phase velocity takes supersonic values for frequencies over 750 Hz. Since θ_c tends to $\pi/4$ and the phase velocity is faster than c_0 at $f_{r\star}$, diffusive waves propagating at an effective supersonic velocity are observed. Such phenomenon is impossible to observe in conventional porous materials. Moreover, around 900 Hz, the phase velocity and phase constant of the PLM equal those in lossless air, the phase of the effective speed of sound is close to zero, and the attenuation coefficient is negligible. All of these indicate that around this frequency the PLM is acoustically transparent.

C.   Example 3 – Adjacent atypical bands, $f_r = f_g$

In this example, a PLM with the same geometrical and physical parameters are those quoted at the beginning of this section is considered but the length of the neck and the radius of the cavity of the resonator are now $l_n = 6.02$ mm and $r_a = 9$ mm, respectively. This allows matching the resonance frequencies, i.e. $f_r = f_g = 677$ Hz. The anti-resonance frequencies are $f_a = 610$ Hz and $f_{r\star} = 910$ Hz.

Figure 5 shows the effective dynamic density, compressibility, speed of sound and wave number of the PLM. For frequencies in between f_a and f_r, the phase of the dynamic density tends to $-\pi$, θ_{C} decreases from 0 to $-\pi/2$, the phase of the effective speed of sound approaches $\pi/2$, and a large attenuation coefficient is seen. These features do not conform to those of a true band gap but the phase velocity does take very small values for $f_a < f < f_r$, which also happens up to a frequency approximately equal to the harmonic mean of the band-edge frequencies of $\tilde{\Delta}_d$. As the frequency increases, however, the phase velocity takes negative values, which reflects the existence of regressive waves. This is induced by the smooth phase transition of the effective compressibility due to viscous dissipation.

Around $f_r = f_g$, a jump in the phase velocity is observed, i.e. $\Re(c)$ transitions from a negative local minimum to a positive local peak, while the attenuation coefficient is locally

28

minimum. The phase θ_c follows the opposite trend. At $f = f_r = f_g$ the phase velocity tends to zero while $|c|$ exhibits a local maximum. For frequencies over $f_g = f_r$ and below $f_{r\star}$, a pseudo band gap is observed, which is a consequence of the fact that in such frequency range $\Re(\mathsf{C}) < 0$ and $\Re(\rho) > 0$. For other frequency regions, e.g. $f \ll f_v$ and $f > f_{r\star}$, the trends are as previously discussed.

D. Example 4 – Overlapping atypical bands, $f_r = f_a$

A PLM with a resonator with neck length increased to $l_n = 7.45$ mm and cavity radius $r_a = 9$ mm and the rest of the parameters unchanged is considered. In this case, $f_r = f_a = 610$ Hz, $f_g = 677$ Hz, and $f_{r\star} = 819$ Hz. Figure 6 shows the effective properties of such PLM in comparison with those of the DPM. At $f = f_a = f_r$, $|\rho|$ and $|\mathsf{C}|$ are maximum and θ_ρ and θ_C both tend to $-\pi/2$. Consequently, the magnitude of the speed of sound tends to zero and its phase to $\pi/2$, the phase velocity tends to zero, and a large attenuation coefficient is seen. Over $f_a = f_r$, regressive waves are observed in the double negative region of the PLM. Such behavior is observed up to f_g at which the negative phase velocity takes its smallest value while the attenuation coefficient tends to zero. For higher frequencies, the phase constant is close to zero and the attenuation coefficient presents a wide peak, while the phase velocity starts increasing and takes supersonic values from a frequency close to $f_{r\star}$. Again, at $f_{r\star}$ a diffusive wave travels with supersonic velocity. Moreover, the PLM appears as acoustically transparent at frequencies around 1000 Hz. The trends in other frequency regions are as previously discussed.

E. Example 5 – Overlapping atypical bands, $f_g = f_{r\star}$

In this example, the elasto-inertial characteristic frequencies f_g and $f_{r\star}$ are matched by further increasing the length of Helmholtz resonator's neck to $l_n = 10.95$ mm and setting the radius of the resonator's cavity to $r_a = 9$ mm, while the values of the rest of the parameters remain unchanged. The elasto-inertial characteristic frequencies are $f_g = f_{r\star} = 677$ Hz, $f_a = 610$ Hz, and $f_r = 505$ Hz. This case is illustrated in Figure 7. In the frequency region limited by f_r and $f_g = f_{r\star}$, the phase velocity tends to zero and the attenuation coefficient takes large values but a local minimum is observed within such a region. Moreover, for

frequencies belonging to the double negative frequency region, regressive waves are supported by the PLM. This is reflected by the negative phase velocity and phase constant as well as the monotonically decreasing nature of the attenuation coefficient in such a region.

As predicted in § III C, $|c|$ takes large values and $\theta_c \to \pi/2$ at $f = f_g = f_{r\star}$. At this frequency, a zero phase velocity, zero phase constant and a minimum in attenuation coefficient are observed, i.e. the large value of $|c|$ is determined by the imaginary part of the effective speed of sound. It is also worth stressing that around $f = f_g = f_{r\star}$, a jump in phase velocity stands out as a feature, while over such frequency a supersonic phase velocity, together with $\theta_c \to 0$, is reached.

F. Example 6 – Adjacent atypical bands, $f_{r\star} = f_a$

By keeping constant the parameters of the PLM but setting $l_n = 13.5$ mm and $r_a = 9$ mm, the anti-resonance frequencies are matched, i.e. $f_{r\star} = f_a = 610$ Hz. The resonance frequencies are $f_g = 677$ Hz and $f_r = 455$ Hz. Figure 8 shows the same frequency-dependent parameters as in, for example, Fig. 7.

For frequencies $f \ll f_v$ the behavior of the effective acoustical properties of the PLM is similar to that of the DPM. In the frequency range $f_r < f < f_{r\star}$, a pseudo band gap is observed, reflected by the large attenuation coefficient and slow phase velocity, together with θ_c approaching $\pi/2$ within such a frequency range. At $f_{r\star} = f_a$, $\theta_c \to \pi/2$ and $|c|$ exhibits a local minimum due to the larger magnitude of ρ in comparison with that of C. Moreover, the phase velocity crosses the zero axis and a local maximum of the attenuation coefficient is achieved. Over $f_{r\star} = f_a$ and below f_g, the real part of the dynamic density is negative while $\Re(\mathsf{C})$ is positive. Despite this, regressive waves travel in the PLM, which further states that such a peculiar behavior does not only occur in double negative frequency bands. In the present case, such a behavior is determined by the smooth transitions in θ_ρ and θ_C primarily caused by viscous dissipation. Moreover, such regressive waves slowly travel through the material and are significantly attenuated, as quantified through the magnitudes of the phase velocity and attenuation coefficient. It is clear that strong dispersion in PLM is observed and its acoustic behavior is different from that of conventional single or multi porosity materials.

30
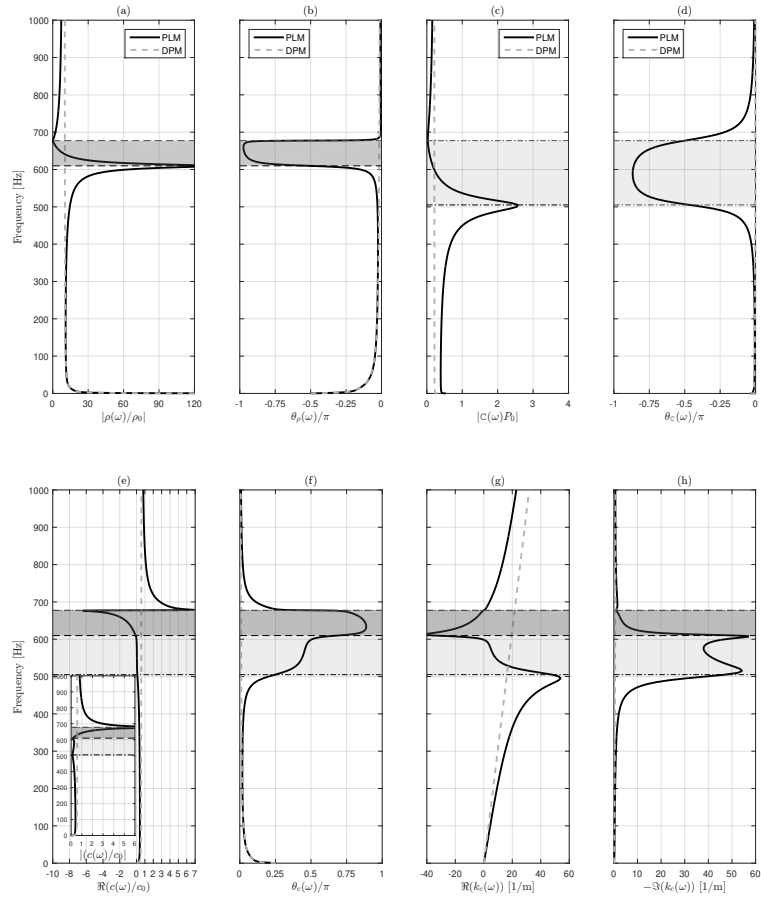
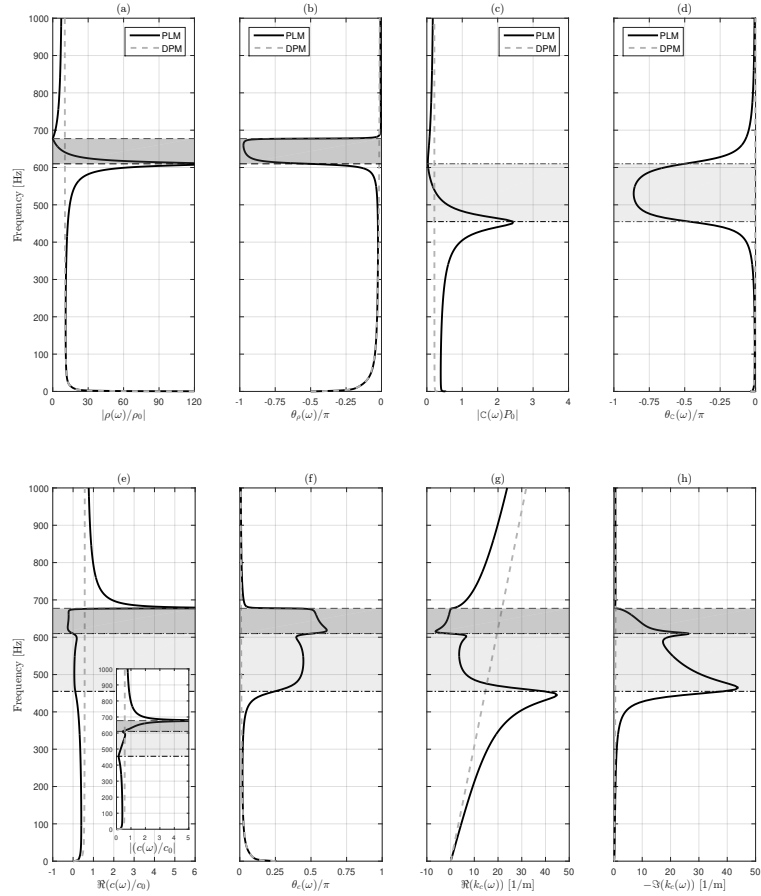FIG. 3: Non overlaping atypical bands. Top: Magnitude and normalized phase of the normalized dynamic density $\rho(\omega)/\rho_0$ [(a) and (b)] and compressibility $\mathsf{C}(\omega)P_0$ [(c) and (d)]. Bottom: Real part [(e)] and phase [(f)] of the effective speed of sound and real part of the wave number [(g)] and attenuation coefficient [(h)]. The inset plot in [(e)] shows the absolute value of the effective speed of sound. Continuous black lines – Permeable lossy metamaterial (PLM). Dashed gray lines – Double porosity material (DPM). The shaded regions represent the atypical frequency bands $\tilde{\Delta}_d = (f_a, f_g)$ [dark gray] and $\tilde{\Delta}_b = (f_r, f_{r\star})$ [light gray].

31

Physics of Fluids

FIG. 4: Overlapping atypical bands. Top: Magnitude and normalized phase of the normalized dynamic density $\rho(\omega)/\rho_0$ [(a) and (b)] and compressibility $C(\omega)P_0$ [(c) and (d)]. Bottom: Real part [(e)] and phase [(f)] of the effective speed of sound and real part of the wave number [(g)] and attenuation coefficient [(h)]. The inset plot in [(e)] shows the absolute value of the effective speed of sound. Continuous black lines – Permeable lossy metamaterial (PLM). Dashed gray lines – Double porosity material (DPM). The shaded regions represent the atypical frequency bands $\tilde{\Delta}_d = (f_a, f_g)$ [dark gray] and $\tilde{\Delta}_b = (f_r, f_{r\star})$ [light gray].

FIG. 5: Adjacent atypical bands, $f_r = f_g$. Top: Magnitude and normalized phase of the normalized dynamic density $\rho(\omega)/\rho_0$ [(a) and (b)] and compressibility $C(\omega)P_0$ [(c) and (d)] of the permeable lossy metamaterial PLM [continuous black lines] and double porosity material [dashed gray lines]. Bottom: Real part [(e)] and phase [(f)] of the effective speed of sound and real part of the wave number [(g)] and attenuation coefficient [(h)]. The inset plot in [(e)] shows the absolute value of the effective speed of sound. The shaded regions represent the frequency bands $(f_a, f_g = f_r)$ [dark gray] and $(f_r = f_g, f_{r\star})$ [light gray].

33

FIG. 6: Overlapping atypical bands, $f_r = f_a$. Top: Magnitude and normalized phase of the normalized dynamic density $\rho(\omega)/\rho_0$ [(a) and (b)] and compressibility $\mathsf{C}(\omega)P_0$ [(c) and (d)] of the permeable lossy metamaterial PLM [continuous black lines] and double porosity material [dashed gray lines]. Bottom: Real part [(e)] and phase [(f)] of the effective speed of sound and real part of the wave number [(g)] and attenuation coefficient [(h)]. The inset plot in [(e)] shows the absolute value of the effective speed of sound. The shaded regions represent the frequency bands $(f_a = f_r, f_g)$ [dark gray] and $(f_r = f_a, f_{r\star})$ [light gray].

34

FIG. 7: Overlapping atypical bands, $f_g = f_{r\star}$. Top: Magnitude and normalized phase of the normalized dynamic density $\rho(\omega)/\rho_0$ [(a) and (b)] and compressibility $C(\omega)P_0$ [(c) and (d)] of the permeable lossy metamaterial PLM [continuous black lines] and double porosity material [dashed gray lines]. Bottom: Real part [(e)] and phase [(f)] of the effective speed of sound and real part of the wave number [(g)] and attenuation coefficient [(h)]. The inset plot in [(e)] shows the absolute value of the effective speed of sound. The shaded regions represent the frequency bands $(f_a, f_g = f_{r\star})$ [dark gray] and $(f_r, f_{r\star} = f_g)$ [light gray].

35

FIG. 8: Adjacent atypical bands, $f_{r\star} = f_a$. Top: Magnitude and normalized phase of the normalized dynamic density $\rho(\omega)/\rho_0$ [(a) and (b)] and compressibility $\mathsf{C}(\omega)P_0$ [(c) and (d)] of the permeable lossy metamaterial PLM [continuous black lines] and double porosity material [dashed gray lines]. Bottom: Real part [(e)] and phase [(f)] of the effective speed of sound and real part of the wave number [(g)] and attenuation coefficient [(h)]. The inset plot in [(e)] shows the absolute value of the effective speed of sound. The shaded regions represent the frequency bands $(f_a = f_{r\star}, f_g)$ [dark gray] and $(f_r, f_{r\star} = f_a)$ [light gray].

G.   Example 7 – Matching f_g and f_r and strong visco-elasto-inertial interaction

Up until now, the microstructural parameters of the permeo-elastic domain and the width of the slit-like channel in Ω_{bf} have not been varied. Because of the former, the dynamic density has been the same for all the examples. By modifying some parameters of the microstructure of the PLM, strong visco-elasto-inertial interaction can be observed. In figure 9, the effective parameters of a PLM exhibiting such interaction are shown. The microstructural parameters of the PLM that have been varied are (see Fig. 2): the height of the gap that connects the front and back fluid-saturated parts of the permeo-elastic channel $h_g = 0.15$ mm, the width of the channel loaded by the acoustic resonator $h_b = 0.3$ mm, and the radius of the cavity and the length and radius of the neck of the acoustic resonator, i.e. $r_a = 9$ mm, $l_n = 17.05$ mm, and $r_n = 2.5$ mm, respectively. In this case, the characteristic frequencies can only be determined from their general, implicit definition. For instance, the apparent viscous characteristic (or Biot) frequency f_v is defined as the frequency at which $|\Im(\mathcal{K}(\omega_v))|/|\Re(\mathcal{K}(\omega_v))| \rightarrow 1$. This definition is compatible with that used for conventional porous materials and results in $f_v = 273$ Hz. An interesting feature of this case is that the elastic power of the films also contributes to the imaginary part of the dynamic permeability. Also, the apparent Biot frequency is mostly determined by the viscous characteristic frequency of the equivalent fluid saturating Ω_{bf}. In a similar manner, the apparent anti-resonance frequency f_a is determined from its implicit definition, given by Eq. (47), with viscous effects accounted for. This characteristic frequency corresponds to the lower boundary of the band where $\Re(\rho) < 0$. Furthermore, f_a, which in this example is low, is strongly affected by the characteristic pore size $\ell_b = O(\sqrt{\phi_b \mathcal{K}_b})$ of the domain Ω_{bf}. If ℓ_b is large in comparison with $\ell_d = O(\sqrt{\phi_d \mathcal{K}_d})$, then the width of the atypical band where $\Re(\rho) < 0$ can be significantly reduced. Note also that $f_{r\star}$ is also affected by ℓ_b through ϕ_b [see Eq. (64)] and for this example is $f_{r\star} = 946$ Hz. In contrast to that, and as expected, the resonance frequencies f_g and f_r, which are matched in this example and equal to 675 Hz, are not significantly affected by h_g and h_b, respectively.

Figures 9a–b show the real part and phase of the dynamic density of the PLM as well as those of SPM and PEM [see Fig. 2]. In SPM, the fluid-saturated part of its REV is Ω_{bf} and the rest of it is perfectly rigid and impermeable, i.e. the only permeable part of its REV is the fluid-saturated channel of width h_b. In PEM, the REV comprises the permeo-elastic

37

channel Ω_{df} and the rest of it is perfectly rigid and impermeable.

Figure 9a shows that the real part of the dynamic density of PEM is negative, with a large magnitude, up to f_g. Recalling that $\Re(\rho_d) = -\eta\Im(\mathcal{K}_d)/\omega|\mathcal{K}_d|^2$ with $\Im(\mathcal{K}_d) = -\phi_d\mathcal{I}_d + \phi_d\mathcal{E}_d$, it is clear that $\Re(\rho_d) < 0$ is observed because the elasticity of the films dominates over the inertia of the fluid-film system. On the contrary, the real part of the dynamic density of SPM, given by $\Re(\rho_b) = \eta\mathcal{I}_b/\omega|\mathcal{K}_b|^2$, is positive, as for any conventional porous material. The real part of the dynamic density of the PLM, given by $\Re(\rho) = -\eta\Im(\mathcal{K})/\omega|\mathcal{K}|^2$ with $\Im(\mathcal{K}) = -\phi_b\mathcal{I}_b - \phi_d\mathcal{I}_d + \phi_d\mathcal{E}_d$, is negative because the effective elastic effects dominate over the inertial effects of the whole fluid-film system. Moreover, at low frequencies, i.e. $f \ll f_v$, $\Re(\rho)$ takes values in between those of $\Re(\rho_d)/\phi_d$ and $\Re(\rho_b)/\phi_b$, which is consistent with the fact that the two pore fluid networks work in parallel in terms of oscillatory flow in them [see Eq. (32)]. However, for frequencies around f_g, the elastic and inertial effects in the permeo-elastic channel compensate each other and the dynamic permeability of the permeo-elastic domain $\mathcal{K}_d$, whose magnitude is maximum at f_g, determines the dynamic permeability of the PLM as well as its dynamic density.

Figure 9b reveals that the phases of the dynamic density of SPM and PEM, $\theta_\rho^{\mathrm{SPM}}$ and $\theta_\rho^{\mathrm{PEM}}$, are rather different, and that of the PLM, i.e. θ_ρ, is influenced by both $\theta_\rho^{\mathrm{SPM}}$ and $\theta_\rho^{\mathrm{PEM}}$ for frequencies up to f_g. It is noted that $\theta_\rho^{\mathrm{SPM}}$ varies from $-\pi/2$ to 0, while $\theta_\rho^{\mathrm{PEM}}$ decreases from $-\pi/2$ down to $-\pi$ at f_g. The former is a classical behavior, which it is not the case for the latter primarily due to the dominance of the elastic effects over inertial ones, as well as that of viscous dissipation in Ω_{df} resulting in the large magnitude of $\Im(\rho_d/\phi_d)$. This, together with the strong contribution of viscous effects in Ω_{bf} accounted for by $\Im(\rho_b/\phi_b)$, is inherited by the phase of the dynamic density of the PML up to f_g. For frequencies over f_g, $\theta_\rho \to 0$, which reflects that viscous effects are negligible in such a frequency range. Physically, the values of the phase of the dynamic density of the PLM reflect that the effective movement of the fluid and the driving force are in quadrature at low frequencies, opposite for frequencies in between approximately 500 Hz and f_g in this example, and in phase for frequencies over f_g. Such a behavior, together with that of the effective compressibility [see Fig. 9c–d] whose behavior has been tuned so that the resonance frequency induced by the Helmholtz resonator f_r matches the resonance frequency of the fluid-film system f_g, has direct consequences on the atypical effective speed of sound and wave number of the PLM, as shown in Figs. 9e–h. For $f \ll f_v$, slow phase velocity is observed, together with increasing attenuation coefficient

38

and a $\pi/4$ phase of the effective speed of sound. This is characteristic of a fluid flow regime determined by viscous effects, which in this case are attributed to the viscous dissipation that occurs in Ω_{bf}. As the frequency increases, slow sound propagation is still observed, the attenuation coefficient exhibits a wide peak centered just over f_v, and θ_c transitions from $\pi/4$ to $\pi/2$, which means that the sound waves are overdamped. For frequencies closer to $f_g = f_r$, anomalous wave propagation and regressive waves are predicted, as it is evidenced by the negative phase velocity and phase constant. However, the attenuation coefficient rapidly decreases in such a frequency region. Within the frequency band $(f_r, f_{r\star})$, a pseudo band gap is observed, where the phase velocity takes small positive values, the phase constant is quasi constant (outside the band transition regions), and the attenuation coefficient is large enough to guarantee significant sound attenuation but decreases as the frequency increases within the band. Over f_g, the phase velocity takes supersonic values, the phase of the effective speed of sound decreases from $\pi/4$ towards zero, the phase constant grows quasi linearly, and the attenuation coefficient decreases. All of these trends physically mean that a wave traveling in the PLM used as an example here is i) progressive, diffusive, and slow at low frequencies; ii) progressive, overdamped, and slow as the frequency increases; iii) regressive, anomalous, weakly attenuated, and relatively fast in frequencies just below $f_g = f_r$; iv) progressive, overdamped, and slow for frequencies over f_g; v) progressive, diffusive, and supersonic at around $f_{r\star}$; and vi) progressive, weakly damped, and supersonic at frequencies over $f_{r\star}$ and up until the highest frequency considered in this example.

Other interesting features of PLMs are worth highlighting. For the sake of brevity, these are now discussed without showing results graphically.

Remarks:

i) In all the examples, the mechanical parameters of the films have been kept constant. Their influence on ρ_d have been discussed in [36, 37] and is as follows. Increasing the "plate" modulus E of the films leads to higher f_{ad} and f_{gd}. This also happens when the films are stretched further by increasing the tension per unit length $\mathcal{T}$. Decreasing the surface density $\rho_e t$ lowers both f_{ad} and f_{gd}. Moreover, a permeo-elastic material with small surface density exhibits a wider atypical band. It shall be emphasized that these trends are observed when the flow regime is determined by elasto-inertial effects. For the case of comparable viscous, elastic, and inertial effects, the trends are similar to those shown in Fig. 9a–b for the PEM material. It should, however, be noted that by varying the parameters that determine the effective

elasticity of the films $\Re(\rho_d)$ can exhibit either negative, zero, or positive values in a wide frequency range, as shown in the figure 9 in [37]. All of these trends are also seen in the dynamic density of a PLM, with the particularity being that the existence of the decoupled pore fluid network Ω_{bf} provides an additional degree of freedom. Indeed, by decreasing the width of the channel h_b of Ω_{bf} the anti-resonance frequency f_a, which is generally larger than f_{ad}, can be lowered; while the opposite trend is observed as h_b is increased, up to a point where the band (f_a, f_g) may become very narrow, meaning that $\Re(\rho)$ takes negative values in a limited frequency band.

ii) The REV of the PLM used as example features a Helmholtz resonator and a clamped film modeled as a Love-Kirchhoff plate under tension. However, the theory is applicable to a PLM with a REV featuring a quarter-wavelength and a film modeled as a membrane for which bending effects are negligible. In this type of PLM, the difference between the first and second resonance frequencies is smaller than that of the PLMs used in the examples. This certainly leads to the possibility of achieving atypical acoustic behavior in different frequency regions where, for example, the atypical band induced by the first anti and resonance frequencies of one type of resonators can overlap with that induced by the second anti and resonance frequencies of the other type of resonators. The analysis in such a case becomes rather complicated and, as such, a simpler PLM has been chosen to exemplify the developed theory.

iii) We ought to mention that the study of the effective group and energy transport velocities in permeable lossy metamaterials is a rich subject that is a matter left to further work, as it also is the physical realization of metamaterial prototypes that can enable the experimental verification of the upscaled theory introduced in this work. Such a prototype building is envisaged to require a significant degree of precision due to the high sensitivity of the effective parameters to the microstructural parameters of the PLM.
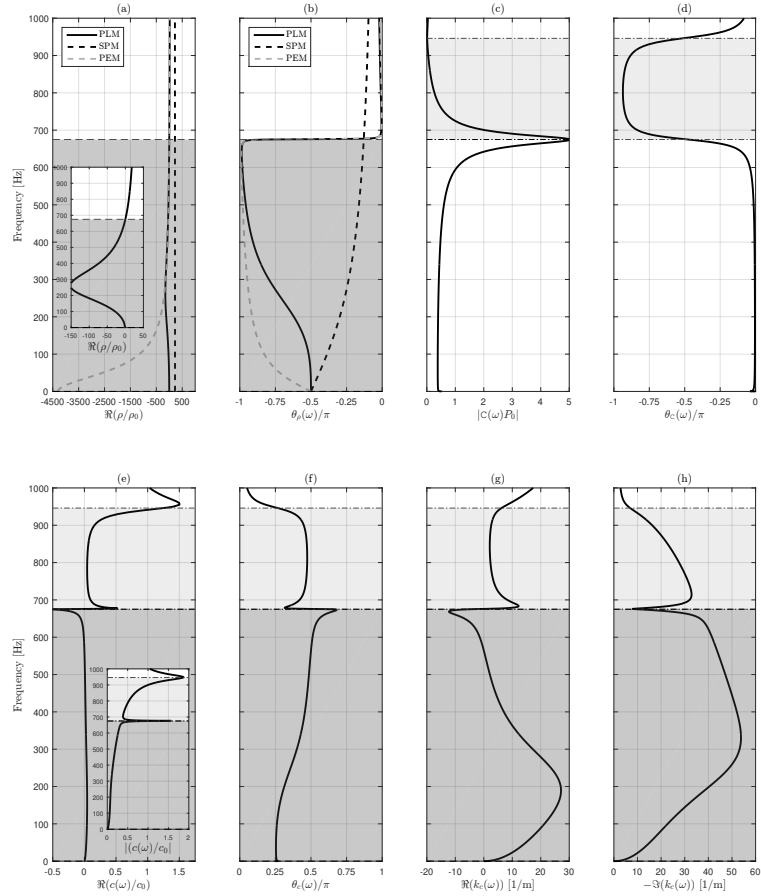
FIG. 9: Matching f_g and f_r and strong visco-elasto-inertial interaction. Top: Real part and normalized phase of the normalized dynamic density $\rho(\omega)/\rho_0$ [(a) and (b)] of the PLM [continuous black lines], SPM [dashed black lines], and PEM [dashed gray lines] [see the text for their description and Fig. 2]; and magnitude and phase of the normalized dynamic compressibility $\mathsf{C}(\omega)P_0$ [(c) and (d)] of the PLM. The inset plot in [(a)] zooms in the frequency region where $\Re(\rho) < 0$. Bottom: Phase velocity [(e)], phase of the effective speed of sound [(f)], phase constant [(g)], and attenuation coefficient [(h)] of the PLM. The inset plot in [(e)] shows the absolute value of the effective speed of sound. The shaded regions represent the frequency bands $(f_a, f_g = f_r)$ [dark gray] and $(f_r = f_g, f_{r\star})$ [light gray].

41

VI.   CONCLUSIONS

Acoustic wave propagation in permeable lossy metamaterials (PLM) was investigated in this paper. The representative elementary volume of the investigated periodic PLM comprised a perfectly rigid and impervious solid domain and two independent pore fluid networks. The fluid that saturates one of the connected pore fluid networks was in contact with the fluid that saturates an acoustic resonator. A thin elastic film is present in the other connected pore fluid network and strongly interacts with the fluid that saturates it.

The two-scale asymptotic homogenization method was used to establish the macroscopic equations that govern sound propagation in PLM. These upscaled equations demonstrated that the PLM can be modeled as an equivalent fluid with unconventional frequency-dependent and complex-valued effective dynamic visco-elasto-inertial permeability (or density) and compressibility. The dynamic visco-elasto-inertial permeability was shown to be a weighted sum of the dynamic permeabilities of the fluid that saturates the pore fluid networks. One of these dynamic permeabilities behave conventionally, while the other is strongly affected by the local fluid-film interaction. In a similar manner, it was proven that the effective compressibility of the PLM is a weighted sum of the effective compressibilities of the fluid that saturates the pore fluid networks. One of these corresponds to a combination of a classical effective compressibility and an apparent compressibility that is dependent on the effective admittance of the acoustic resonator, while the other behaves in a conventional manner. The strong fluid-film interaction was shown to determine the atypical behavior of the effective dynamic density, while the acoustic resonators determine that of the effective compressibility. The result of this are two atypical bands which could overlap or not, or be adjacent. The positions and boundaries of these bands are determined by elasto-inertial characteristic frequencies which can be tuned by varying microstructural and/or physical parameters. In each atypical band the real part of one of the effective parameters is negative.

Sub-wavelength band gaps, slow sound, supersonic diffusive waves, and regressive waves, among others, are all phenomena present in PLM. Their physical origin was established from the analysis of the effective parameters and their links with the fields that determine sound propagation in the PLM locally. Moreover, an hybrid (numerical-analytical) model for the effective acoustical properties of the PLM was developed and used to exemplify the possible

variations in the atypical acoustic behavior of the PLM. This also allowed highlighting the crucial role of losses and the need to properly account for them in the modeling of PLM.

This work has shown that the propagation of acoustic waves in PLM is primarily determined by classical visco-thermal dissipation and inner elasto-inertial resonances induced by decoupled acoustic and elastic resonators. It also provides a theoretical framework for the rational design of PLM for acoustic wave manipulation. Accounting for the interaction between two different types of resonators would be a logical extension of the theory presented. In addition, the experimental verification of the theory would be a subject of future work.

ACKNOWLEDGMENTS

DATA AVAILABILITY

The data that support the findings of this study are available from the corresponding author upon reasonable request.

Appendix A: UPSCALING OF THE WAVE EQUATION IN PERMEABLE LOSSY METAMATERIALS

1. Physical analysis and rescaled local description

The aim of the physical analysis is to determine both the variables in Eqs. (1)–(20) that fluctuate either locally or macroscopically and the relative order of magnitude of the terms in the said equations. Such analysis is crucial for the rescaling of the local description.

The equations formulated in Ω_{bf} are analyzed first. Such analysis is well established (see, e.g., [43, 44, 48]). Let us recall that, in the long-wavelength regime, the macroscopic pressure gradient drives the fluid flow in Ω_{bf}. This leads to following estimate $|\nabla p_b| = O\left(\breve{p}_b/L\right)$, where, from now on, the accent $\breve{\ }$ indicates a characteristic value of the term it is applied

43

to (e.g. $\check{p}_b$ is a characteristic value of p_b). In addition, the fluid velocity and its rate of deviatoric deformation fluctuate locally, i.e. $|\text{div}(2\eta\mathbf{D}(\mathbf{v}_b))| = O(\eta\check{v}_b/l^2)$, while its divergence varies with the sound wavelength, i.e. $|\nabla \cdot \mathbf{v}_b| = O(\check{v}_b/L)$. On the other hand, the excess temperature in Eq. (3) varies locally, which leads to $|\kappa\nabla \cdot \nabla\tau_b| = O(\kappa\check{\tau}_b/l^2)$.

Regarding the relative order of magnitude of the terms, it is of interest to describe the acoustic behavior for the case where all the terms in Eqs. (1)–(3) contribute to the local fluid flow and heat conduction. This means that in the equation of conservation of momentum the viscous and inertial terms as well as the pressure gradient are of the same order of magnitude, i.e. $O(\eta\check{v}_b/\ell^2) = O(\rho_0\omega\check{v}_b) = O(\check{p}_b/L)$, in the equation of conservation of mass one has that $O(\check{v}_b/L) = O(\omega\check{\rho}_b/\rho_0)$, and in the equation of conservation of energy the conduction and the thermal inertia terms are balanced by the source due to pressure, i.e. $O(\kappa\check{\tau}_b/l^2) = O(\omega\rho_0 c_p\check{\tau}_b) = O(\omega\check{p}_b)$. Moreover, in the equation of state the following estimate holds $O(\check{p}_b/P_0) = O(\check{\rho}_b/\rho_0) = O(\check{\tau}_b/\tau_0)$.

The physical analysis for the set of equations (1)–(9) is completed by assessing the boundary conditions. Specifically, the continuity of pressure on Γ_{rf} sets $O(\check{p}_b) = O(\check{p}_r)$ while the long-wavelength condition imposes that the mass flux pulsed from the resonator on Γ_{rf} is of one order smaller than the mass flux produced by the incident wave in the fluid network, i.e. $|\rho_0\mathbf{v}_r \cdot \mathbf{n}|/|\rho_0\mathbf{v}_b \cdot \mathbf{n}| = O(\varepsilon)$. Such an estimate can be justified by considering a cell Ω_b, denoting the ingoing mass flux on one of its faces (of surface S_b) as $S_b\rho_0\check{v}_{b1}$, the outgoing mass flux on the opposite face as $S_b\rho_0\check{v}_{b2}$, and the mass flux pulsed from the resonator as $O(\rho_0\check{v}_r\Gamma_{rf})$. Recalling that, by hypothesis, one has that $L \gg l$, then $(S_b\rho_0\check{v}_{b2} - S_b\rho_0\check{v}_{b1})/S_b\rho_0\check{v}_{b1} \approx l/L$. Moreover, the conservation of mass imposes that $S_b\rho_0\check{v}_{b2} \approx S_b\rho_0\check{v}_{b1} + \Gamma_{rf}\rho_0\check{v}_r$. It then follows that $\Gamma_{rf}\check{v}_r/S_b\check{v}_{b1} = O(\varepsilon)$. On the other hand, invoking the continuity of thermal flux one obtains $\check{\tau}_r/\check{\tau}_b = O(\varepsilon)$, which is a valid approximation as long a characteristic size of the resonator (e.g. a radius of the neck of a Helmholtz resonator) is of one order smaller than l.

The physical analysis of the Eqs. (10)–(13), which are formulated in Ω_{df}, closely follows that developed in previous paragraphs for the Eqs. (1)–(4). Hence, it suffices replacing the subscript b by d. The physical analysis of the equations that govern the dynamics of the film, i.e. Eqs. (14)–(18), and associated boundary conditions is now addressed by recalling the results in [36, 37]. The continuity of the fluid and film velocities, i.e. Eq. (17), provides the estimate $O(\check{v}_d) = O(\omega\check{u}_d)$, which imposes that the film velocity varies locally, as the out-of-plane shear stress vector $\mathbf{T}$ and in-plane stress tensor $\mathbf{M}$ also do. Then, to account for

44

visco-elasto-inertial fluid-film interaction, the order of magnitude of the terms in the equation of conservation of momentum (14) should satisfy $O(EI\check{u}_d/l^4) = O(\rho_e t\omega^2\check{u}_d) = O(\eta\check{v}_d/l) = O(\check{p}_dl/L)$. In addition, the local variations of the deviatoric viscous stress determine that its jump across Γ also fluctuates locally. It then follows that $O([\eta\check{v}_d/l]) = O(\eta\check{v}_d/l)$. Finally, since the pressure varies with the wavelength, its jump across Γ is estimated as $O([\check{p}_d]/l) = O(\check{p}_d/L)$.

2. Rescaled local description

The two-scale asymptotic homogenization method for periodic media is used to establish an equivalent macroscopic model for acoustic wave propagation in permeable lossy metamaterials. The use of this method is possible due to the large scale separation between the local and macroscopic characteristic sizes, i.e. $l/L = \varepsilon \ll 1$. To represent the evolution at the two spatial scales and taking the macroscopic characteristic size as a reference length, one can introduce the following dimensional space variables: $\boldsymbol{x}$ and $\boldsymbol{y} = \varepsilon^{-1}\boldsymbol{x}$, which respectively account for macro- and microscopic fluctuations. Then, the usual differential operator ∇ becomes $\nabla_x + \varepsilon^{-1}\nabla_y$. Note that the spatial variables can be considered as independent due to the large separation of scales and non-bold letters for the spatial variables are used to ease the notation.

The use of two space variables is combined with a rescaling of the usual equations based upon a single space variable and the physical analysis that allowed to determine the relative order of magnitude among the terms. In particular, the rescaling of the equations enables to have consistency between the magnitude of the gradient of a quantity Q and the respective physical estimate. This is based on the fact that the actual physical gradient of a quantity $Q(x,y)$ that varies macroscopically is of the order of $\nabla_x Q$, which is expressed when using the two introduced spatial variables as $\nabla_x Q + \varepsilon^{-1}\nabla_y Q$. Instead, the actual physical gradient of a quantity that fluctuates locally is of the order of $\nabla_y Q$, and this is expressed as $\varepsilon(\nabla_x Q + \varepsilon^{-1}\nabla_y Q)$ which introduces the rescaling by the scale ratio ε. As an example, $\text{div}(\mathbf{D}(\mathbf{v}_b))$ must be rewritten as $\varepsilon^2\text{div}(\mathbf{D}(\mathbf{v}_b))$ in order to express that the fluid velocity varies locally.

The rescaled local equations are given by (with $\nabla = \nabla_x + \varepsilon^{-1}\nabla_y$ and $\iota = b, d$)

$$\varepsilon^2\text{div}(2\eta\mathbf{D}(\mathbf{v}_\iota)) - \nabla p_\iota = \mathrm{j}\omega\rho_0\mathbf{v}_\iota \quad \text{in} \quad \Omega_{\iota f}, \tag{A.1}$$

$$j\omega\rho_\iota + \rho_0\nabla\cdot\mathbf{v}_\iota = 0 \quad \text{in} \quad \Omega_{\iota f}, \tag{A.2}$$

$$\varepsilon^2\kappa\nabla\cdot\nabla\tau_\iota = j\omega\rho_0 c_p\tau_\iota - j\omega p_\iota \quad \text{in} \quad \Omega_{\iota f}, \tag{A.3}$$

$$\frac{p_\iota}{P_0} = \frac{\rho_\iota}{\rho_0} + \frac{\tau_\iota}{\tau_0} \quad \text{in} \quad \Omega_{\iota f}, \tag{A.4}$$

$$\mathbf{v}_\iota = \mathbf{0} \quad \text{on} \quad \Gamma_{\iota s}, \tag{A.5}$$

$$\tau_\iota = 0 \quad \text{on} \quad \Gamma_{\iota s}\cup\Gamma, \tag{A.6}$$

$$\rho_0\mathbf{v}_b\cdot\mathbf{n} = \varepsilon\rho_0\mathbf{v}_r\cdot\mathbf{n} \quad \text{on} \quad \Gamma_{rf}, \tag{A.7}$$

$$p_b = p_r \quad \text{on} \quad \Gamma_{rf}, \tag{A.8}$$

$$\tau_b = \varepsilon\tau_r \quad \text{on} \quad \Gamma_{rf}, \tag{A.9}$$

$$\varepsilon\widetilde{\nabla}\cdot(\mathbf{T} + \mathcal{T}\varepsilon\widetilde{\nabla}u_d) = -\omega^2\rho_e t u_d - [(2\eta\varepsilon\mathbf{D}(\mathbf{v}_d) - \varepsilon^{-1}p_d\mathbf{I})\cdot\mathbf{N}]\cdot\mathbf{N} \quad \text{on} \quad \Gamma, \tag{A.10}$$

$$\mathbf{T} = -\varepsilon\widetilde{\text{div}}(\mathbf{M}) \quad \text{on} \quad \Gamma, \tag{A.11}$$

$$\mathbf{M} = EI\left((1-\nu)\varepsilon^2\widetilde{\mathbf{e}}(\widetilde{\nabla}u_d) + \nu\varepsilon^2\widetilde{\nabla}\cdot\widetilde{\nabla}u_d\mathbf{I}\right) \quad \text{on} \quad \Gamma, \tag{A.12}$$

$$\mathbf{v}_d = j\omega u_d\mathbf{N} \quad \text{on} \quad \Gamma, \tag{A.13}$$

$$u_d = 0 \quad \text{and} \quad \varepsilon\widetilde{\nabla}u_d\cdot\mathbf{n} = 0 \quad \text{on} \quad \partial\Gamma. \tag{A.14}$$

3.   Boundary-value problems

The unknown variables written as series expansions in ε, e.g. $p_b(x,y) = \sum_{k=0}^{\infty}\varepsilon^k p_b^{(k)}(x,y)$, are inserted in the rescaled local equations. Then, matching the terms with equal powers of ε leads to boundary-value problems whose solution enables the determination of the effective parameters of the permeable lossy metamaterial.

Identifying the ε^{-1}-term in Eqs. (A.1) and (A.10) leads to $\nabla_y p_b^{(0)} = \nabla_y p_d^{(0)} = \mathbf{0}$ and $[p_d^{(0)}] = 0$. Hence, the leading-order pressures are, consistently with the physical analysis, macroscopic variables, i.e. $p_b^{(0)} = p_b^{(0)}(x)$ and $p_d^{(0)} = p_d^{(0)}(x)$. The boundary value problems arising from homogenization are directly presented in what follows.

46

a. Oscillatory fluid flow in Ω_{bf}

For the oscillatory Stokes problem, consider the Hilbert space $\mathcal{W}_b$ of complex $\Omega-$periodic velocity fields $\mathbf{w}_b$ defined in Ω_{bf} that fulfils $\nabla_y \cdot \mathbf{w}_b = 0$ in Ω_{bf} and $\mathbf{w}_b = 0$ on Γ_{bs}. Then, the weak formulation (see [43]) is given by

$$\forall \mathbf{w}_b \in \mathcal{W}_b, \quad A_b(\mathbf{v}_b^{(0)}, \mathbf{w}_b) = B_b(\mathbf{w}_b), \tag{A.15}$$

with

$$B_b(\mathbf{w}_b) = -\nabla_x p_b^{(0)} \cdot \langle \overline{\mathbf{w}_b} \rangle_b, \tag{A.16}$$

$$A_b(\mathbf{v}_b^{(0)}, \mathbf{w}_b) = \eta \mathfrak{R}_b(\mathbf{v}_b^{(0)}, \mathbf{w}_b) + \mathrm{j}\omega\rho_0 \mathfrak{I}_b(\mathbf{v}_b^{(0)}, \mathbf{w}_b), \tag{A.17}$$

where

$$\mathfrak{R}_b(\mathbf{v}_b^{(0)}, \mathbf{w}_b) = \langle 2\mathbf{D}_y(\mathbf{v}_b^{(0)}) : \mathbf{D}_y(\overline{\mathbf{w}_b}) \rangle_b, \tag{A.18}$$

$$\mathfrak{I}_b(\mathbf{v}_b^{(0)}, \mathbf{w}_b) = \langle \mathbf{v}_b^{(0)} \cdot \overline{\mathbf{w}_b} \rangle_b. \tag{A.19}$$

In these equations, the spatial averaging operator is defined as

$$\langle \cdot \rangle_b = \frac{1}{\Omega_{bf}} \int_{\Omega_{bf}} \cdot d\Omega. \tag{A.20}$$

Relying on the properties of the form A_b (i.e. sesquilinear and coercive in $\mathcal{W}_b$) and the semi-linearity of B_b, the existence and uniqueness of the solution of the linear problem Eq. (A.15) is ensured by the Lax-Milgram theorem. Moreover, since the forcing term is $\nabla_x p_b^{(0)}$, the solution $\mathbf{v}_b^{(0)}$ can be written as

$$\mathbf{v}_b^{(0)} = -\frac{\hat{\mathbf{k}}_b(y, \omega)}{\eta} \cdot \nabla_x p_b^{(0)}, \tag{A.21}$$

where $\hat{\mathbf{k}}_b$ represents a Ω-periodic normalized local velocity field.

b. Oscillatory heat conduction in Ω_{bf}

Regarding the oscillatory heat conduction problem, its weak formulation is obtained by multiplying Eq. (A.3) identified at $\varepsilon^{(0)}$ by the conjugate of a $\Omega-$periodic test function $q_b \in H^1$ that satisfies the boundary condition $q_b = 0$ on $\Gamma_{bs} \cup \Gamma_{rf}$, integrating by part, applying the divergence theorem, and considering the periodicity. The final result is

$$\forall q_b \in H^1, \quad a_b(\tau_b^{(0)}, q_b) = b_b(q_b), \tag{A.22}$$

47

where

$$b_b(q_b) = j\omega p_b^{(0)} \langle \overline{q}_b \rangle_b,$$ (A.23)

$$a_b(\tau_b^{(0)}, q_b) = \kappa \mathbb{H}_b(\tau_b^{(0)}, q_b) + j\omega \rho_0 c_p \mathbb{S}_b(\tau_b^{(0)}, q_b),$$ (A.24)

with

$$\mathbb{H}_b(\tau_b^{(0)}, q_b) = \langle \nabla_y \tau_b^{(0)} \cdot \nabla_y \overline{q}_b \rangle_b,$$ (A.25)

$$\mathbb{S}_b(\tau_b^{(0)}, q_b) = \langle \tau_b^{(0)} \overline{q}_b \rangle_b.$$ (A.26)

The linear problem (A.22) is forced by the locally-constant pressure $p_b^{(0)}$. Hence, $\tau_b^{(0)}$ can be linearly related to $p_b^{(0)}$ via

$$\tau_b^{(0)} = \frac{\hat{\Theta}_b(y, \omega)}{\kappa} j\omega p_b^{(0)},$$ (A.27)

where $\hat{\Theta}_b$ represents a Ω-periodic normalized local temperature field.

c. Oscillatory fluid-film interaction problem in $\Omega_{df} \cup \Gamma$

Focusing on the equations formulated in Ω_{df} and on Γ, the identification process leads to an oscillatory Stokes coupled with the equations that govern the leading-order film velocity $v_d^{(0)} = j\omega u_d^{(0)}$. The associated weak formulation has been obtained in [37] and is therefore only recalled here.

Consider the Hilbert space $\mathcal{W}_d$ of complex $\Omega-$periodic velocity fields $\mathbf{w}_d$ defined in $\Omega_{df} \cup \Gamma$ that fulfil the following kinematic restrictions: $\nabla_y \cdot \mathbf{w}_d = 0$ in Ω_{df}, $\mathbf{w}_d = 0$ on Γ_{ds}, $\mathbf{w}_d = w_d \mathbf{N}$ on Γ, and $w_d = 0$ and $\widetilde{\nabla}_y w_d \cdot \mathbf{n} = 0$ on $\partial\Gamma$. The weak formulation is given by

$$\forall \mathbf{w}_d \in \mathcal{W}_d, \quad A_d(\mathbf{v}_d^{(0)}, \mathbf{w}_d) = B_d(\mathbf{w}_d),$$ (A.28)

with

$$B_d(\mathbf{w}_d) = -\nabla_x p_d^{(0)} \cdot \langle \overline{\mathbf{w}_d} \rangle_d,$$ (A.29)

$$A_d(\mathbf{v}_d^{(0)}, \mathbf{w}_d) = \eta \Re_d(\mathbf{v}_d^{(0)}, \mathbf{w}_d) + j\omega \varrho \Im_d(\mathbf{v}_d^{(0)}, \mathbf{w}_d) + \frac{\mathfrak{K}}{j\omega} \mathfrak{E}_d(v_d^{(0)}, w_d),$$ (A.30)

where

$$\Re_d(\mathbf{v}_d^{(0)}, \mathbf{w}_d) = \langle 2\mathbf{D}_y(\mathbf{v}_d^{(0)}) : \mathbf{D}_y(\overline{\mathbf{w}_d}) \rangle_d,$$ (A.31)

$$\Im_d(\mathbf{v}_d^{(0)}, \mathbf{w}_d) = \frac{\rho_0}{\varrho} \Im_f(\mathbf{v}_d^{(0)}, \mathbf{w}_d) + \frac{\rho_e t}{\varrho} \Im_p(v_d^{(0)}, w_d),$$ (A.32)

$$\mathfrak{E}_d(v_d^{(0)}, w_d) = \frac{\mathcal{T}}{\mathfrak{K}} \mathfrak{E}_m(v_d^{(0)}, w_d) + \frac{EI}{\mathfrak{K}} \mathfrak{E}_p(v_d^{(0)}, w_d),$$ (A.33)

48

with

$$\mathfrak{I}_f(\mathbf{v}_d^{(0)}, \mathbf{w}_d) = \langle \mathbf{v}_d^{(0)} \cdot \overline{\mathbf{w}_d} \rangle_d, \tag{A.34a}$$

$$\mathfrak{I}_p(v_d^{(0)}, w_d) = \langle v_d^{(0)} \overline{w_d} \rangle_\Gamma, \tag{A.34b}$$

$$\mathfrak{E}_m(v_d^{(0)}, w_d) = \langle \widetilde{\nabla}_y v_d^{(0)} \cdot \widetilde{\nabla}_y \overline{w_d} \rangle_\Gamma, \tag{A.34c}$$

$$\mathfrak{E}_p(v_d^{(0)}, w_d) = \langle \widetilde{\mathcal{N}}(v_d^{(0)}, w_d) \rangle_\Gamma, \tag{A.34d}$$

$$\widetilde{\mathcal{N}}(v_d^{(0)}, w_d) = (1 - \nu)\widetilde{\mathbf{e}}_y(\widetilde{\nabla}_y v_d^{(0)}) : \widetilde{\mathbf{e}}_y(\widetilde{\nabla}_y \overline{w_d}) + \nu \widetilde{\nabla}_y \cdot \widetilde{\nabla}_y v_d^{(0)} \widetilde{\nabla}_y \cdot \widetilde{\nabla}_y \overline{w_d}. \tag{A.35}$$

In these equations, the spatial averaging operators are given by

$$\langle \cdot \rangle_d = \frac{1}{\Omega_{df}} \int_{\Omega_{df}} \cdot \ d\Omega. \quad \text{and} \quad \langle \cdot \rangle_\Gamma = \frac{1}{\Omega_{df}} \int_\Gamma \cdot \ d\Gamma, \tag{A.36}$$

and the density parameter ϱ and the elastic parameter $\mathfrak{K}$ that accounts for both bending and membrane effects are given by

$$\varrho = \rho_0 + \rho_e t \frac{\Gamma}{\Omega_{df}} \quad \text{and} \quad \mathfrak{K} = \frac{EI/\Gamma + \mathcal{T}}{\Omega_{df}}. \tag{A.37}$$

Since the form A_d is sesquilinear and coercive in $\mathcal{W}_d$ and B_d is semi-linear, the Lax-Milgram theorem ensures the existence and uniqueness of the solution of $\mathbf{v}_d^{(0)}$ in Ω_{df} and, by continuity, that of $v_d^{(0)}$ on Γ. Furthermore, being Eq. (A.28) linear and recalling that the system is forced by the macroscopic pressure gradient, it is direct to write the solution as

$$\mathbf{v}_d^{(0)} = -\frac{\hat{\mathbf{k}}_d(y, \omega)}{\eta} \cdot \nabla_x p_d^{(0)} \quad \text{in} \quad \Omega_{df}, \tag{A.38a}$$

$$v_d^{(0)} \mathbf{N} = \mathbf{v}_d^{(0)} \quad \text{on} \quad \Gamma. \tag{A.38b}$$

Despite the formal similarity between the dynamic Darcy's law Eq. (A.21) and Eq. (A.38a), it is stressed that the latter is fundamentally different due to the fact that the Ω-periodic normalized local velocity field $\hat{\mathbf{k}}_d$ accounts for visco-elasto-inertial instead of only visco-inertial effects, as $\hat{\mathbf{k}}_b$ does.

d.   Oscillatory heat conduction in Ω_{df}

The weak formulation of the oscillatory heat conduction problem in Ω_b is obtained by replacing the subscripts b by d in Eqs. (A.22)–(A.27) of §A 3 b. The solution of the oscillatory heat conduction in Ω_{df} is also given by Eq. (A.27) but with $b \to d$.

49

4. Derivation of the macroscopic equations

The identification of the ε^0 terms in Eq. (A.2), with $\iota = b$, yields

$$\nabla_x \cdot \mathbf{v}_b^{(0)} + \nabla_y \cdot \mathbf{v}_b^{(1)} + \mathrm{j}\omega\frac{\rho_b^{(0)}}{\rho_0} = 0, \tag{A.39}$$

which after applying the operator Eq. (A.20) and using Eq. (A.4) at ε^0 becomes

$$\nabla_x \cdot \langle \mathbf{v}_b^{(0)}\rangle_b + \langle \nabla_y \cdot \mathbf{v}_b^{(1)}\rangle_b + +\mathrm{j}\omega\langle\frac{p_b^{(0)}}{P_0} - \frac{\tau_b^{(0)}}{\tau_0}\rangle_b = 0. \tag{A.40}$$

In this equation, the term $\langle \nabla_y \cdot \mathbf{v}_b^{(1)}\rangle_b$ is calculated by using the divergence theorem, noting that the surface integrals on opposite boundaries of the unit cell cancel out due to periodicity, and using Eq. (A.7) at ε^1 and Eq. (A.5) at ε^0. The final result is

$$\langle \nabla_y \cdot \mathbf{v}_b^{(1)}\rangle_b = \mathrm{j}\omega p_b^{(0)}\frac{2}{\mathcal{L}}\frac{\mathcal{Y}_r(\omega)}{\mathrm{j}\omega}, \tag{A.41}$$

where $\mathcal{L} = 2\Omega_{bf}/\Gamma_{rf}$ is a characteristic length and the effective admittance $\mathcal{Y}_r$ of the resonator is given by

$$\mathcal{Y}_r(\omega) = \frac{1}{\Gamma_{rf}}\int_{\Gamma_{rf}}\frac{\mathbf{v}_r^{(0)}\cdot\mathbf{n}}{p_b^{(0)}}d\Gamma. \tag{A.42}$$

Inserting Eqs. (A.27) and (A.41) into Eq. (A.39) and recalling the thermodynamic identity $P_0/\tau_0 = \rho_0 c_p(\gamma - 1)/\gamma$ (with γ being the adiabatic exponent), one obtains

$$\nabla_x \cdot \langle \mathbf{v}_b^{(0)}\rangle_b + \mathrm{j}\omega p_b^{(0)}\mathsf{C}_{br} = 0, \tag{A.43}$$

where the effective compressibility C_{br} is given by Eq. (26).

The identification of the ε^0 terms in Eq. (A.2) (for $\iota = d$) and application of the spatial averaging operator Eq. (A.36) to the resulting equation yields

$$\nabla_x \cdot \langle \mathbf{v}_d^{(0)}\rangle_d + \langle \nabla_y \cdot \mathbf{v}_d^{(1)}\rangle_d = -\mathrm{j}\omega\langle\frac{\rho_d^{(0)}}{\rho_0}\rangle_d. \tag{A.44}$$

In this equation, the term $\langle \nabla_y \cdot \mathbf{v}_d^{(1)}\rangle_d$ is null due to $\mathbf{v}_d^{(1)} = 0$ on Γ_s, periodicity, and the continuity of the fluid velocity across the interface Γ; while the right-hand side term is linked with the effective compressibility of the fluid saturating Ω_{df}. Taking into account these two remarks, Eq. (A.44) becomes

$$\nabla_x \cdot \langle \mathbf{v}_d^{(0)}\rangle_d + \mathrm{j}\omega p_d^{(0)}\mathsf{C}_d(\omega) = 0. \tag{A.45}$$

The macroscopic mass balance Eq. (21) is obtained by adding Eqs. (A.43) and (A.45) after having multiplied them by ϕ_b and ϕ_d, respectively. The macroscopic constitutive fluid flow law Eq. (22) is obtained from Eqs. (A.21) and (A.38). In both macroscopic equations, the overall leading-order velocity, defined as $\mathbf{V}^{(0)} = \mathbf{v}_\iota^{(0)}$ in $\Omega_{\iota f}$ (with $\iota = b, d$), has been spatially averaged over the whole REV using the operator $\langle \cdot \rangle = \Omega^{-1} \int_{\Omega_{bf} \cup \Omega_{df}} \cdot \, d\Omega$.

Appendix B: Expressions for the effective admittance of acoustic resonators

For a quarter-wavelength resonator, the effective admittance is given by

$$\mathcal{Y}_r = \mathcal{Y}_{rq} = \frac{1}{-\mathrm{j} Z_{cr} \cot{(k_{cr} d_r)}}, \tag{B.1}$$

where d_r is the depth resonator and Z_{cr} and k_{cr} are, respectively, the characteristic impedance and wave number of the effective fluid that saturates it. For a lossless, tortuous quarter-wavelength resonator, one has that the characteristic impedance is given by $Z_{cr} = \rho_0 c_0 \sqrt{\alpha_{\infty r}}/\phi_r$, where $\alpha_{\infty r}$ and ϕ_r are, respectively, the inner tortuosity and porosity of the resonator; and the wave number is given by $k_{cr} = k_0 \sqrt{\alpha_{\infty r}} = \omega \sqrt{\alpha_{\infty r}}/c_0$, where c_0 is the speed of sound in the saturating gas. On the other hand, it is clear from Eq. (B.1) that $\mathcal{Y}_r \to \infty$ when $\cot{(k_{cr} d_r)} \to 0$. For a lossless resonator, this occurs when $k_{cr} d_r = n\pi/2$ (with $n = 1, 3, ...$). Hence the first resonance ($n = 1$) occurs at $f_r = c_0/4d\sqrt{\alpha_{\infty r}}$.

For a Helmholtz resonator with neck length l_n, neck constant cross-section $\Gamma_{rn} = \Gamma_{rf}$, neck volume Ω_n, cavity length h_a, cavity constant cross-section Γ_{ra}, and cavity volume Ω_a; the effective admittance is given by (with $\mathcal{G} = \Gamma_{ra}/\Gamma_{rn}$)

$$\mathcal{Y}_r = \mathcal{Y}_{rh} = \frac{Z_{wa} + Z_{wn}\mathcal{G}}{Z_{wn} Z_{wa} + Z_{cn}^2 \mathcal{G}}, \tag{B.2}$$

with

$$Z_{wa} = -\mathrm{j} Z_{ca} \cot{(k_{ca} h_a)} \quad \text{and} \quad Z_{wn} = -\mathrm{j} Z_{cn} \cot{(k_{cn} l_n)}, \tag{B.3}$$

where Z_{ca} and k_{ca} (respectively Z_{cn} and k_{cn}) are the characteristic impedance and the wave number of the fluid saturating the cavity (respectively the neck), which for a cavity and a neck where losses are negligible equal, in both cases, to Z_0 and k_0. Moreover, one can make use of asymptotic values of the effective parameters to estimate the resonance frequency as $f_r = c_0 \Gamma_{rn}/\sqrt{\Omega_a \Omega_n}$.

Appendix C: Link between the effective parameters and local fields

1. Dynamic permeabilities and densities

To simplify the analysis, macro-isotropy or a preferential flow direction is considered. This means that the involved tensors are replaced by scalars.

a. Oscillatory flow in Ω_{bf}

The relationship between the dynamic visco-inertial permeability $\mathcal{K}_b$ and the local velocity field is identified by taking the solution of the oscillatory flow problem described in § A 3 a as a test field, i.e. $\mathbf{w}_b = \mathbf{v}_b$. Note that the superscript indicating the order has been dropped to alleviate the notation. After evaluating this solution in the weak formulation (A.15), taking the conjugate, and recalling that for a preferential flow direction $\langle \mathbf{v}_b \rangle_b = -(\mathcal{K}_b/\eta)\nabla p_b$, one obtains a direct relationship between the dynamic visco-inertial permeability and the frequency-dependent local flow in the period. This reads as

$$\mathcal{K}_b = \eta \frac{\overline{A_b(\mathbf{v}_b, \mathbf{v}_b)}}{|\nabla p_b|^2} = \mathcal{K}_b^{\Re} + j\mathcal{K}_b^{\Im}, \tag{C.1}$$

with

$$\mathcal{K}_b^{\Re} = \frac{\Re(\mathbf{v}_b, \mathbf{v}_b)}{|\nabla p_b/\eta|^2} = \Re(\hat{\mathbf{k}}_b, \hat{\mathbf{k}}_b) \geq 0, \tag{C.2}$$

$$\mathcal{K}_b^{\Im} = -\delta_v^{-2} \frac{\Im_b(\mathbf{v}_b, \mathbf{v}_b)}{|\nabla p_b/\eta|^2} = -\frac{\Im_b(\hat{\mathbf{k}}_b, \hat{\mathbf{k}}_b)}{\delta_v^2} \leq 0, \tag{C.3}$$

where $\delta_v = \sqrt{\eta/\rho_0 \omega}$ is the viscous boundary layer thickness.

Hence, the dynamic visco-inertial permeability can be written as (with $\mathcal{V}_b = \Re(\hat{\mathbf{k}}_b, \hat{\mathbf{k}}_b) \geq 0$ and $\mathcal{I}_b = \delta_v^{-2}\Im_b(\hat{\mathbf{k}}_b, \hat{\mathbf{k}}_b) \geq 0$)

$$\mathcal{K}_b = \mathcal{V}_b - j\mathcal{I}_b. \tag{C.4}$$

This equation shows that the real and imaginary parts $\mathcal{K}_b$ reflect the dissipated viscous and kinetic energies developed by the flow (for a unitary pressure gradient).

The dynamic density $\rho_b = \eta/j\omega\mathcal{K}_b$ can be conveniently written as

$$\rho_b = -\frac{\eta}{\omega} \frac{G(\mathcal{K}_b^{\star})}{\mathcal{K}_b^{\Re}} \left(1 + \frac{j}{\mathcal{K}_b^{\star}}\right) \quad \text{with} \quad G(q) = \frac{q}{1+q^2}, \tag{C.5}$$

and $\mathcal{K}_b^{\star} = \mathcal{K}^{\Im}/\mathcal{K}^{\Re} = -\mathcal{I}_b/\mathcal{V}_b$.

52

b. Oscillatory fluid-film interaction in $\Omega_{df} \cup \Gamma$

The procedure to obtain the link between the dynamic visco-elasto-inertial permeability $\mathcal{K}_d$ and the local fields is similar to the one detailed in the previous subsection. For the sake of brevity, only the final result is provided, i.e.

$$\mathcal{K}_d = \mathcal{V}_d + \mathrm{j}(\mathcal{E}_d - \mathcal{I}_d), \tag{C.6}$$

where

$$\mathcal{V}_d = \frac{\mathfrak{R}_d(\mathbf{v}_d, \mathbf{v}_d)}{|\nabla p_d / \eta|^2} = \mathfrak{R}_d(\hat{\mathbf{k}}_d, \hat{\mathbf{k}}_d) \geq 0, \tag{C.7}$$

$$\mathcal{E}_d = \frac{\mathfrak{K}}{\eta\omega} \frac{\mathfrak{E}_d(v_d, v_d)}{|\nabla p_d / \eta|^2} = \frac{\mathfrak{K}}{\eta\omega} \mathfrak{E}_d(\hat{k}_d, \hat{k}_d) = \frac{\mathcal{T}\mathfrak{E}_m(\hat{k}_d, \hat{k}_d) + EI\mathfrak{E}_p(\hat{k}_d, \hat{k}_d)}{\eta\omega} \geq 0, \tag{C.8}$$

$$\mathcal{I}_d = \delta_v^{-2} \frac{\varrho}{\rho_0} \frac{\mathfrak{I}_d(\mathbf{v}_d, \mathbf{v}_d)}{|\nabla p_d / \eta|^2} = \frac{\varrho}{\rho_0} \frac{\mathfrak{I}_d(\hat{k}_d, \hat{k}_d)}{\delta_v^2} = \frac{\mathfrak{I}_f(\hat{\mathbf{k}}_d, \hat{\mathbf{k}}_d) + \frac{\rho_e t}{\rho_0} \mathfrak{I}_p(\hat{k}_d, \hat{k}_d)}{\delta_v^2} \geq 0. \tag{C.9}$$

Eq. (C.6) shows that $\mathcal{K}_d$ reflects the dissipated viscous, kinetic and elastic (or pseudo-elastic) energies developed by the oscillatory fluid flow which is strongly affected by the fluid-film interaction. In particular, the kinetic energy is determined by the inertia of the fluid and the films while the elastic (or pseudo-elastic) energy by bending and membrane effects in the films.

The dynamic density $\rho_d = \eta/\mathrm{j}\omega\mathcal{K}_d$ is obtained by replacing the subscript b by d in Eq. (C.5), i.e.

$$\rho_d = -\frac{\eta}{\omega} \frac{G(\mathcal{K}_d^\star)}{\mathcal{K}_d^\Re} \left(1 + \frac{\mathrm{j}}{\mathcal{K}_d^\star}\right), \tag{C.10}$$

where $\mathcal{K}_d^\star = \mathcal{K}_d^\Im / \mathcal{K}_d^\Re = (\mathcal{E}_d - \mathcal{I}_d)/\mathcal{V}_d$.

c. Oscillatory flow in the permeable lossy metamaterial

Combining the previous results, one can write the visco-elasto-inertial permeability as

$$\mathcal{K} = \phi_b \mathcal{V}_b + \phi_d \mathcal{V}_d + \mathrm{j}(\phi_d \mathcal{E}_d - [\phi_b \mathcal{I}_b + \phi_d \mathcal{I}_d]). \tag{C.11}$$

This equation shows that the viscous dissipated, kinetic and elastic (or pseudo-elastic) energies developed by the flows in Ω_{df} and Ω_{bf} affect the overall permeability of the permeable lossy metamaterial.

53

The dynamic density is then given by Eq. (32), which for a preferential propagation direction becomes

$$\rho(\omega) = \left(\frac{\phi_b}{\rho_b(\omega)} + \frac{\phi_d}{\rho_d(\omega)} \right)^{-1} = -\frac{\eta}{\omega} \frac{G(\mathcal{K}^\star)}{\mathcal{K}^\Re} \left(1 + \frac{\mathrm{j}}{\mathcal{K}^\star} \right) \tag{C.12}$$

where $\mathcal{K}^\star = \mathcal{K}^\Im / \mathcal{K}^\Re = (\phi_d \mathcal{E}_d - [\phi_b \mathcal{I}_b + \phi_d \mathcal{I}_d]) / (\phi_b \mathcal{V}_b + \phi_d \mathcal{V}_d)$.

2. Dynamic thermal permeabilities, compressibilities, and effective admittance

The relationship between the effective parameter $\Theta_b(\omega)$ and the local temperature field $\tau_b = \tau_b^{(0)}$ is now identified. To do so, let us take the solution itself as a test field, i.e. $q_b = \tau_b$, and evaluate it in the conjugate of Eq. (A.22) to obtain (note that we have dropped the superscript indicating the order to alleviate the notation)

$$\overline{a_b(\tau_b, \tau_b)} = -\mathrm{j}\omega \overline{p}_b \langle \tau \rangle_b. \tag{C.13}$$

Recalling that $\langle \tau_b \rangle_b = (\Theta_b / \kappa) \mathrm{j} \omega p_b$, one obtains a direct relationship between the dynamic thermal permeability and the frequency-dependent local temperature field in the period, which reads as

$$\Theta_b = \frac{\kappa \overline{a_b(\tau_b, \tau_b)}}{|\omega p_b|^2} = \Theta_b^\Re + \mathrm{j} \Theta_b^\Im, \tag{C.14}$$

where

$$\Theta_b^\Re = \frac{\mathbb{H}_b(\tau_b, \tau_b)}{|\omega p_b / \kappa|^2} = \mathbb{H}_b(\hat{\Theta}_b, \hat{\Theta}_b) \geq 0, \tag{C.15}$$

$$\Theta_b^\Im = -\delta_t^{-2} \frac{\mathbb{S}_b(\tau_b, \tau_b)}{|\omega p_b / \kappa|^2} = -\frac{\mathbb{S}_b(\hat{\Theta}_b, \hat{\Theta}_b)}{\delta_t^2} \leq 0, \tag{C.16}$$

and $\delta_t = \sqrt{\kappa / \omega \rho_0 c_p}$ the thermal boundary layer thickness.

Hence the effective compressibility C_b can be written as

$$\mathsf{C}_b = \frac{1}{P_0} [(1 - \mathcal{S}_b) - \mathrm{j} \mathcal{H}_b] = \mathsf{C}_b^\Re + \mathrm{j} \mathsf{C}_b^\Im, \tag{C.17}$$

where

$$\mathcal{H}_b = \frac{\gamma - 1}{\gamma} \frac{\Theta_p^\Re}{\delta_t^2} = \frac{\gamma - 1}{\gamma} \frac{\mathbb{H}_b(\hat{\Theta}_b, \hat{\Theta}_b)}{\delta_t^2} \geq 0, \tag{C.18}$$

$$\mathcal{S}_b = -\frac{\gamma - 1}{\gamma} \frac{\Theta_b^\Im}{\delta_t^2} = \frac{\gamma - 1}{\gamma} \frac{\mathbb{S}_b(\hat{\Theta}_b, \hat{\Theta}_b)}{\delta_t^4} \geq 0. \tag{C.19}$$

54

To link the local temperature field in Ω_{df} with the effective parameters, the same steps as in the previous paragraphs are followed. The final results are obtained by replacing the subscript b by d in Eqs. (C.14)–(C.18).

The overall effective compressibility is then linked to the local fields as well as the effective admittance of the resonator $\mathcal{Y}_r = \mathcal{Y}_r^{\Re} + \mathrm{j}\mathcal{Y}_r^{\Im}$, via

$$\mathsf{C}(\omega) = \left[\frac{\phi_b}{P_0}(1 - \mathcal{S}_b) + \phi_b \frac{2}{\mathcal{L}}\frac{\mathcal{Y}_r^{\Im}}{\omega} + \frac{\phi_d}{P_0}(1 - \mathcal{S}_d)\right] - \mathrm{j}\left[\frac{\phi_b}{P_0}\mathcal{H}_b + \phi_b \frac{2}{\mathcal{L}}\frac{\mathcal{Y}_r^{\Re}}{\omega} + \frac{\phi_d}{P_0}\mathcal{H}_d\right]. \quad \text{(C.20)}$$

[1] G. Ma and P. Sheng. "Acoustic metamaterials : From local resonances to broad horizons," Sci. Adv. **2** (2), e1501595 (2016).

[2] S. A. Cummer, J. Christensen, and A. Alù. "Controlling sound with acoustic metamaterials," Nat. Rev. Mater. **1**, 16001 (2016).

[3] G. Liao, C. Luan, Z. Wang, J. Liu, X. Yao, and J. Fu, "Acoustic metamaterials: a review of theories, structures, fabrication approaches, and applications," Adv. Mater. Technol. **6**, 2000787 (2021).

[4] Z. Liu, X. Zhang, Y. Mao, Y. Y. Zhu, Z. Yang, C. T. Chan, and P. Sheng, "Locally resonant sonic materials," Science **289**, 1734–1736 (2000).

[5] N. Fang, D. Xi, J. Xu, M. Ambati, W. Srituravanich, C. Sun, and X. Zhang, "Ultrasonic metamaterials with negative modulus," Nat. Mater. **5**, 452–456 (2006).

[6] Y. Ding, Z. Liu, C. Qiu, and J. Shi. "Metamaterial with simultaneously negative bulk modulus and mass density," Phys. Rev. Lett. **99**, 093904 (2007).

[7] Y. Cheng, J. Y. Xu, and X. J. Liu. "One-dimensional structured ultrasonic metamaterials with simultaneously negative dynamic density and modulus," Phys. Rev. B **77** (4), 045134 (2008).

[8] S. H. Lee, C. M. Park, Y. M. Seo, Z. G. Wang, and C. K. Kim, "Composite acoustic medium with simultaneously negative density and modulus," Phys. Rev. Lett. **104**, 054301 (2010).

[9] F. Bongard, H. Lissek, and J. R. Mosig. "Acoustic transmission line metamaterial with negative/zero/positive refractive index," Phys. Rev. B **82** (9), 094306 (2010).

[10] L. Fok and X. Zhang. "Negative acoustic index metamaterial," Phys. Rev. B **83** (21), 214304 (2011).

[11] Y. M. Seo, J. J. Park, S. H. Lee, C. M. Park, C. K. Kim, S. H. Lee, "Acoustic metamaterial

exhibiting four different sign combinations of density and modulus," J. Appl. Phys. **111**, 023504 (2012).

[12] Z. Liang, M. Willatzen, J. Li, and J. Christensen. "Tunable acoustic double negativity metamaterial," Sci. Rep. **2** (1), 859 (2011).

[13] S. H. Lee and O. B. Wright, "Origin of negative density and modulus in acoustic metamaterials," Phys. Rev. B **93**, 024302 (2016).

[14] V. C. Henríquez, V. M. García-Chocano, and J. Sánchez-Dehesa, "Viscothermal losses in double-negative acoustic metamaterials,". Phys. Rev. Appl. **8**, 014029 (2017).

[15] C. Bellis and B. Lombard, "Simulating transient wave phenomena in acoustic metamaterials using auxiliary fields", Wave Motion **86**, 175–194 (2019).

[16] H. Jia, M. Ke, R. Hao, Y. Ye, F. Liu, and Z. Liu, "Subwavelength imaging by a simple planar acoustic superlens," Appl. Phys. Lett. **97** (17), 173507 (2010).

[17] Y. Li, G. Yu, B. Liang, X. Zou, G. Li, S. Cheng, and J. Cheng, "Three-dimensional ultrathin planar lenses by acoustic metamaterials," Sci. Rep. **4** (1), 6830 (2014).

[18] X. Yang, J. Yin, G. Yu, L. Peng, and N. Wang, "Acoustic superlens using helmholtz-resonator-based metamaterials," Appl. Phys. Lett. **107** (19), 193505 (2015).

[19] S. L. Zhai, X. P. Zhao, S. Liu, F. L. Shen, L. L. Li, and C. R. Luo, "Inverse doppler effects in broadband acoustic metamaterials," Sci. Rep. **6** (1), 32388 (2016).

[20] S. H. Lee, C. M. Park, Y. M. Seo, and C. K. Kim, "Reversed Doppler effect in double negative metamaterials," Phys. Rev. B **81** (24), 241102 (2010).

[21] T. Dupont, P. Leclaire, O. Sicot, X. L. Gong, and R. Panneton, "Acoustic properties of air-saturated porous materials containing dead-end porosity," J. Appl. Phys. **110**, 094903 (2011).

[22] X. Jiang, B. Liang, R.-Q. Li, X.-Y Zou, L.-L. Yin, and J.-C. Cheng. "Ultra-broadband absorption by acoustic metamaterials," Appl. Phys. Lett. **105**, 243505 (2014).

[23] J.-P. Groby, A. Lardeau, W. Huang, and Y. Auregan, "The use of slow sound to design simple sound absorbing materials," J. Appl. Phys. **117**, 124903 (2015).

[24] N. Jiménez, W. Huang, V. Romero-García, V. Pagneux, and J.-P. Groby, "Ultra-thin metamaterial for perfect and quasiomnidirectional sound absorption," Appl. Phys. Lett. **109**, 121902 (2016).

[25] D. C. Brooke, O. Umnova, P. Leclaire, T. Dupont "Acoustic metamaterial for low frequency sound absorption in linear and nonlinear regimes," J. Sound Vib. **485**, 115585 (2020).

[26] A. O. Krushynska, F. Bosia, M. Miniaci, and N. M. Pugno, "Spider web-structured labyrinthine acoustic metamaterials for low-frequency sound control," New J. Phys. **19**, 105001 (2017).

[27] Y. Li and B. M. Assouar. "Acoustic metasurface-based perfect absorber with deep subwavelength thickness," Appl. Phys. Lett. **108**, 063502 (2016).

[28] C. Chen, Z. Du, G. Hu, and J. Yang. "A low-frequency sound absorbing material with subwavelength thickness," Appl. Phys. Lett. **110**, 221903 (2017).

[29] Y. Shen, Y. Yang, X. Guo, Y. Shen, and D. Zhang, "Low-frequency anechoic metasurface based on coiled channel of gradient cross-section," Appl. Phys. Lett. **114**, 083501 (2019).

[30] F. Wu, Y. Xiao, D. Yu, H. Zhao, Y. Wang, and J. Wen, "Low-frequency sound absorption of hybrid absorber based on micro-perforated panel and coiled-up channels," Appl. Phys. Lett. **114**, 151901 (2019).

[31] Z. Yang, J. Mei, M. Yang, N. Chan, and P. Sheng. "Membrane-type acoustic metamaterial with negative dynamic mass," Phys. Rev. Lett. **101**, 204301 (2008).

[32] C. J. Naify, C.-M. Chang, G. McKnight, and S. Nutt. "Transmission loss and dynamic response of membrane-type locally resonant acoustic metamaterials," J. App. Phys. **108**, 114905 (2010).

[33] J. Mei, G. Ma, M. Yang, Z. Yang, and W. Wen. "Dark acoustic metamaterials as super absorbers for low-frequency sound," Nat. Commun. **3**, 756 (2012).

[34] C. Boutin, "Acoustics of porous media with inner resonators," J. Acoust. Soc. Am. **134**(6), 4717–4729 (2013).

[35] C. Boutin, and F. X. Bécot, "Theory and experiments on poro-acoustics with inner resonators," Wave Motion **54**, 76–99 (2015).

[36] R. Venegas and C. Boutin, "Acoustics of permeo-elastic materials," J. Fluid Mech. **828**, 135–174 (2017).

[37] C. Boutin and R. Venegas, "Pore-scale bending and membrane effects in permeo-elastic media," Mech. Mater. **145**, 103362 (2020).

[38] N. J. R. K. Gerard and Y. Jing, "Loss in acoustic metasurfaces: a blessing in disguise," MRS Commun. **10**, 32–41 (2020).

[39] C. Zwikker and C. W. Kosten, Sound absorbing materials (Elsevier, 1949).

[40] M. A. Biot, "Theory of propagation of elastic waves in a fluid-saturated porous solid. I. Low-frequency range," J. Acoust. Soc. Am. **28**, 168–178 (1956).

[41] M. A. Biot, "Theory of propagation of elastic waves in a fluid-saturated porous solid. II. Higher

frequency range," J. Acoust. Soc. Am. **28**, 179–191 (1956).

[42] J. F. Allard and N. Atalla, Propagation of Sound in Porous Media: Modeling Sound Absorbing Materials (John Wiley & Sons, 2009) 2nd ed.

[43] J. L. Auriault, C. Boutin, and C. Geindreau, Homogenization of Coupled Phenomena in Heterogeneous Media (ISTE Ltd and John Wiley & Sons, 2009).

[44] J. L. Auriault, L. Borne, and R. Chambon, "Dynamics of porous saturated media, checking of the generalized law of Darcy," J. Acoust. Soc. Am. **77**, 1641–1650 (1985).

[45] D. L. Johnson, J. Koplik, and R. Dashen, "Theory of dynamic permeability and tortuosity in fluid-saturated porous media," J. Fluid Mech. **176**, 379–402 (1987).

[46] Y. Champoux and J. F. Allard, "Dynamic tortuosity and bulk modulus in air-saturated porous media," J. Appl. Phys. **70**, 1975–1979 (1991).

[47] S. R. Pride, F. D. Morgan, and A. F. Gangi, "Drag forces of porous-medium acoustics," Phys. Rev. B **47**, 4964–4975 (1993).

[48] D. Lafarge, P. Lemarinier, J. F. Allard, and V. Tarnow, "Dynamic compressibility of air in porous structures at audible frequencies," J. Acoust. Soc. Am. **102**, 1995–2006 (1997).

[49] M. R. Stinson, "The propagation of plane sound waves in narrow and wide circular tubes, and generalization to uniform tubes of arbitrary cross-sectional shape," J. Acoust. Soc. Am. **89**, 550–558 (1991).

[50] M. Nori and R. Venegas, "Sound propagation in porous materials with annular pores," J. Acoust. Soc. Am. **141**, 4642–4651 (2017).

[51] Z. Xu, W. He, F. Xin, and T. J. Lu, "Sound propagation in porous materials containing rough tubes," Phys. Fluids **32**, 093604 (2020).

[52] J. Ning, Y. Li, and G. Zhao, "Simple multi-sections unit-cell model for sound absorption characteristics of lotus-type porous metals," Phys. Fluids **31**, 077102 (2019).

[53] W. He, M. Liu, X. Peng, F. Xin, and T.-J. Lu, "Sound absorption of petal shaped micro-channel porous materials," Phys. Fluids **33**, 063606 (2021).

[54] K. Attenborough, "Acoustical characteristics of rigid fibrous absorbents and granular materials," J. Acoust. Soc. Am. **73**, 785–799 (1983).

[55] A. M. Chapman and J. J. L. Higdon, "Oscillatory stokes flow in periodic porous media," Phys. Fluids **4**, 2099–2116 (1992).

[56] O. Umnova, K. Attenborough, and K. M. Li, "Cell model calculations of dynamic drag param-

58

eters in packings of spheres," J. Acoust. Soc. Am. **107**, 3113–3119 (2000).

[57] C. Boutin and C. Geindreau, "Estimates and bounds of dynamic permeability of granular media," J. Acoust. Soc. Am. **124**, 3576–3593 (2008).

[58] C. Boutin and C. Geindreau, "Periodic homogenization and consistent estimates of transport parameters through sphere and polyhedron packings in the whole porosity range," Phys. Rev. E **82**, 036313 (2010).

[59] R. Venegas, "Microstructure influence on acoustical properties of multiscale porous materials," Ph.D. thesis (University of Salford, Salford, United Kingdom, 2011).

[60] C. Perrot, F. Chevillotte, and R. Panneton, "Bottom-up approach for microstructure optimization of sound absorbing materials," J. Acoust. Soc. Am. **124**, 940–948 (2008).

[61] O. Umnova, D. Tsiklauri, and R. Venegas, "Effect of boundary slip on the acoustical properties of microfibrous materials," J. Acoust. Soc. Am **126**, 1850–1861 (2009).

[62] T. G. Zieliński, "Microstructure representations for sound absorbing fibrous media: 3d and 2d multiscale modelling and experiments," J. Sound Vib. **409**, 112–130 (2017).

[63] T. G. Zieliński, R. Venegas, C. Perrot, M. Cervenka, F. Chevillotte, and K. Attenborough, "Benchmarks for microstructure-based modelling of sound absorbing rigid-frame porous media," J. Sound Vib. **483**, 115441 (2020).

[64] C. Perrot, F. Chevillotte, and R. Panneton, "Dynamic viscous permeability of an open-cell aluminum foam: Computations versus experiments," J. Appl. Phys. **103**, 024909 (2008).

[65] C. Perrot, F. Chevillotte, M. T. Hoang, G. Bonnet, F.-X. Bécot, L. Gautron, and A. Duval, "Microstructure, transport, and acoustic properties of open-cell foam samples: Experiments and three-dimensional numerical simulations," J. Appl. Phys. **111**, 014911 (2012).

[66] F. Chevillotte and C. Perrot, "Effect of the three-dimensional microstructure on the sound absorption of foams: A parametric study," J. Acoust. Soc. Am. **142**, 940–948 (2017).

[67] J. Ning, G. Zhao, and X. He, "Non-acoustical parameters and sound absorption characteristics of porous polyurethane foams," Phys. Fluids **31**, 037106 (2019).

[68] H. T. Luu, C. Perrot, V. Monchiet, and R. Panneton, "Three-dimensional reconstruction of a random fibrous medium: geometry, transport and sound absorbing properties," J. Acoust. Soc. Am. **141**, 4768–4780 (2017).

[69] J. Ning and Y. Li, "Dynamic flow resistivity and sound absorption of compressed fibrous porous materials: experimental and theoretical," Phys. Fluids **32**, 127103 (2020).

59

[70] J. L. Auriault and C. Boutin. "Deformable porous media with double porosity. III: Acoustics," Transport Porous Med. **14** (2), 143–162 (1994).

[71] C. Boutin, P. Royer, and J. L. Auriault, "Acoustic absorption of porous surfacing with dual porosity," Int. J. Solids Struct. **35**, 4709–4737 (1998).

[72] X. Olny and C. Boutin, "Acoustic wave propagation in double porosity media," J. Acoust. Soc. Am. **113**, 73–89 (2003).

[73] R. Venegas and O. Umnova, "Acoustical properties of double porosity granular materials," J. Acoust. Soc. Am. **130**, 2765–2776 (2011).

[74] R. Venegas and O. Umnova, "Influence of sorption on sound propagation in granular activated carbon," J. Acoust. Soc. Am. **140**, 755–766 (2016).

[75] C. Boutin and R. Venegas, "Assessment of the effective parameters of dual porosity deformable media," Mech. Mater. **102**, 26–46 (2016).

[76] R. Venegas and C. Boutin, "Acoustics of sorptive porous materials," Wave Motion **68**, 162–181 (2017).

[77] R. Venegas, C. Boutin, and O. Umnova, "Acoustics of multiscale sorptive porous materials," Phys. Fluids **29**, 082006 (2017).

[78] R. Venegas and C. Boutin, "Acoustics of permeable heterogeneous materials with local non-equilibrium pressure states," J. Sound Vib. **418**, 221–239 (2018).

[79] R. Venegas and C. Boutin, "Enhancing sound attenuation in permeable heterogeneous materials via diffusion processes," Acta Acust. United Ac. **104**, 623–635 (2018).

[80] E. Gourdon and M. Seppi, "Extension of double porosity model to porous materials containing specific porous inclusions," Acta Acust. United Ac. **96**, 275–291 (2010).

[81] F. Chevillotte, L. Jaouen, and F.-X. Bécot, "On the modeling of visco-thermal dissipations in heterogeneous porous media," J. Acoust. Soc. Am. **138**, 3922–3929 (2015).

[82] R. Venegas, T. G. Zieliński, G. Núñez, and F.-X. Bécot, "Acoustics of porous composites," Compos. B. Eng. **220**, 109006 (2021).

[83] G. Núñez, R. Venegas, T. G. Zieliński, and F.-X. Bécot, "Equivalent fluid approach to modeling the acoustical properties of polydisperse heterogeneous porous composites," Phys. Fluids **33**, 062008 (2021).

[84] A. Tsimpoukis and D. Valougeorgisa, "Pulsatile pressure driven rarefied gas flow in long rectangular ducts," Phys. Fluids **30**, 047104 (2018).

60

Physics of Fluids

[85] K. Pradhan and A. Guha, "Fluid dynamics of oscillatory flow in three-dimensional branching networks," Phys. Fluids **31**, 063601 (2019).

[86] U. Torres-Herrera, "Dynamic permeability of fluids in rectangular and square microchannels: Shift and coupling of viscoelastic bidimensional resonances," Phys. Fluids **33**, 047104 (2021).

[87] M. S. Nagargoje, D. K. Mishra, and R. Gupta, "Pulsatile flow dynamics in symmetric and asymmetric bifurcating vessels," Phys. Fluids **33**, 071904 (2021.)

AIP Publishing

L

l

Ω_{bf}

Ω_b

Ω_r

Ω_{bs}

Ω_d

Ω_{ds}

Ω_{df}

Γ